

SANDIA REPORT

SAND2004-1052

Unlimited Release

Printed 22 March 2004

NEW MECHANISM FOR UPSET OF ELECTRONICS

Robert A. Salazar, Luis L. Molina, Paull E. Patterson, Larry D. Bacon, Guillermo Loubriel

Prepared by

Sandia National Laboratories

Albuquerque, New Mexico 87185 and Livermore, California 94550

Sandia is a multiprogram laboratory operated by Sandia Corporation,
a Lockheed Martin Company, for the United States Department of Energy's
National Nuclear Security Administration under Contract DE-AC04-94AL85000.

Approved for public release; further dissemination unlimited.



Issued by Sandia National Laboratories, operated for the United States Department of Energy by Sandia Corporation.

NOTICE: This report was prepared as an account of work sponsored by an agency of the United States Government. Neither the United States Government, nor any agency thereof, nor any of their employees, nor any of their contractors, subcontractors, or their employees, make any warranty, express or implied, or assume any legal liability or responsibility for the accuracy, completeness, or usefulness of any information, apparatus, product, or process disclosed, or represent that its use would not infringe privately owned rights. Reference herein to any specific commercial product, process, or service by trade name, trademark, manufacturer, or otherwise, does not necessarily constitute or imply its endorsement, recommendation, or favoring by the United States Government, any agency thereof, or any of their contractors or subcontractors. The views and opinions expressed herein do not necessarily state or reflect those of the United States Government, any agency thereof, or any of their contractors.

Printed in the United States of America. This report has been reproduced directly from the best available copy.

Available to DOE and DOE contractors from

U.S. Department of Energy
Office of Scientific and Technical Information
P.O. Box 62
Oak Ridge, TN 37831
Telephone: (865)576-8401
Facsimile: (865)576-5728
E-Mail: reports@adonis.osti.gov
Online ordering: <http://www.doe.gov/bridge>

Available to the public from

U.S. Department of Commerce
National Technical Information Service
5285 Port Royal Rd
Springfield, VA 22161
Telephone: (800)553-6847
Facsimile: (703)605-6900
E-Mail: orders@ntis.fedworld.gov
Online order: <http://www.ntis.gov/orderng.html>



SAND2004-1052
Unlimited Release
Printed March 22, 2004

NEW MECHANISM FOR UPSET OF ELECTRONICS

Robert A. Salazar, Luis L. Molina, Paul E. Patterson, Larry D. Bacon, Guillermo Loubriel
Directed Energy Special Applications Department
Sandia National Laboratories
P.O. Box 5800
Albuquerque, NM 87185-1153

Abstract

For many decades, engineers and scientists have studied the effects of high power microwaves (HPM) on electronics. These studies usually focus on means of delivering energy to upset electronic equipment and ways to protect equipment from HPM. The motivation for these studies is to develop the knowledge necessary either to cause disruption or to protect electronics from disruption. Since electronic circuits must absorb sufficient energy to fail and the source used to deliver this energy is far away from the electronic circuit, the source must emit a large quantity of energy. In free space, for example, as the distance between the source and the target increases, the source energy must increase by the square of distance. The HPM community has dedicated substantial resources to the development of higher energy sources as a result.

Recently, members of the HPM community suggested a new disruption mechanism that could potentially cause system disruptions at much lower energy levels. The new mechanism, based on nonlinear dynamics, requires an expanded theory of circuit operation. This report

summarizes an investigation of electronic circuit nonlinear behavior as it applies to inductor-resistor-diode circuits (known as the Linsay circuit) and phased-locked-loops.

With the improvement in computing power and the need to model circuit behavior with greater precision, the nonlinear effects of circuit have become very important. In addition, every integrated circuit has as part of its design a protective circuit. These protective circuits use some variation of semiconductor junctions that can interact with parasitic components, present in every real system. Hence, the protective circuit can behave as a Linsay circuit.

Although the nonlinear behavior is understandable, it is difficult to model accurately. Many researchers have used classical diode models successfully to show nonlinear effects within predicted regions of operation. However, these models do not accurately predict measured results. This study shows that models based on SPICE, although they exhibit chaotic behavior, do not properly reproduce circuit behavior without modifying diode parameters. This report describes the models and considerations used to model circuit behavior in the nonlinear range of operation. Further, it describes how a modified SPICE diode model improves the simulation results.

We also studied the nonlinear behavior of a phased-locked-loop. Phased-locked loops are fundamental building blocks to many major systems (aileron, seeker heads, etc). We showed that an injected RF signal could drive the phased-locked-loop into chaos. During these chaotic episodes, the frequency of the phased-locked-loop takes excursion outside its normal range of operation. In addition to these excursions, the phased-locked-loop and the system it is controlling requires some time to get back into normal operation. The phased-locked-loop only needs to be upset enough long enough to keep it off balance.

TABLE OF CONTENTS

INTRODUCTION.....	9
NONLINEAR DYNAMICS THEORY.....	10
HISTORY	10
METRICS OF CHAOS	11
DYNAMICAL SYSTEM.....	13
RECONSTRUCTION	14
LYAPUNOV NUMBERS	15
FRACTAL NUMBERS.....	16
POINCARÉ MAPS	18
BIFURCATION.....	18
LINSAY CIRCUIT	19
THEORY AND SIMULATIONS.....	20
SIMULATION RESULTS	22
EXPERIMENTAL RESULTS.....	26
PHASE-LOCKED LOOP	41
PHASE-LOCKED LOOP	42
PHASE-LOCKED LOOP THEORY	42
PHASE-LOCKED LOOP APPLICATION.....	44
REFERENCES.....	63

LIST OF FIGURES

FIGURE 1 THE LINSAY CIRCUIT	10
FIGURE 2 PERIODIC VARIABLE	13
FIGURE 3 PHASE SPACE PLOT	14
FIGURE 4 THE KOCH SNOWFLAKE	17
FIGURE 5 POINCARÉ MAP	18
FIGURE 6 BIFURCATION PLOT	19
FIGURE 7 LINSAY CIRCUIT	20
FIGURE 8 TIME SERIES RESULTS EARLY IN THE SERIES	23
FIGURE 9 TIME SERIES RESULTS LATE IN THE SERIES	24
FIGURE 10 SPECTRAL RESPONSE	24
FIGURE 11 LYAPUNOV RESULTS	25
FIGURE 12 REVERSE RECOVERY	26
FIGURE 13 REVERSE RECOVERY WAVEFORMS	30
FIGURE 14 EXPERIMENT AND SIMULATION RESULTS OF ONE VERSUS EIGHT PULSES	31
FIGURE 15 DIODE 11 CAPACITANCE	31
FIGURE 16 DIODE RESONATOR CIRCUIT COMMONLY REFERRED TO AS THE LINSAY CIRCUIT	32
FIGURE 17 BIFURCATION PLOT	33
FIGURE 18 BIFURCATION PLOT	34
FIGURE 19 SIMULATION BIFURCATION PLOT (UN-SCALED T_{RR})	38
FIGURE 20 SIMULATION BIFURCATION PLOT (SCALED T_{RR})	38
FIGURE 21 DIODES 3, 6, AND 7 FREQUENCY BIFURCATION PLOTS	39
FIGURE 22 DIODES 8, 10, AND 11 FREQUENCY BIFURCATION PLOTS	40
FIGURE 23 FREQUENCY BIFURCATION DETAILS FOR DIODES 3, 6, 10, AND 11	41
FIGURE 24 DIAGRAM OF A PHASE-LOCKED LOOP	42
FIGURE 25 PHASE-PLANE PLOT	43
FIGURE 26 74HC7046A PLL CIRCUIT	45
FIGURE 27 74HC7046A SWEPT FREQUENCY TEST	46
FIGURE 28 MC145220 MOTOROLA EVALUATION BOARD USED TO MEASURE PLL RESPONSE	47
FIGURE 29 MC135220 MOTOROLA EVALUATION BOARD SCHEMATIC	48
FIGURE 30 BLOCK DIAGRAM OF THE RADIO SHACK FRS RADIO RF SECTION	49

FIGURE 31 BLOCK DIAGRAM OF THE TOSHIBA TB31202FN IC THE PLL CHIP.....	50
FIGURE 32 SPECTRAL SHIFTING AND BROADENING.....	50
FIGURE 33 RF PCB SECTION OF RADIO SHACK FRS RADIO.....	51
FIGURE 34 TIME WAVEFORMS OF THE PLL.....	52
FIGURE 35 ERROR VOLTAGE RESPONSE WITH CHANGING DRIVE FREQUENCY (CW).....	53
FIGURE 36 POWER MEASUREMENT LAYOUT.....	54
FIGURE 37 SETUP OF 95GHZ TEST AT 12CM.....	55
FIGURE 38 SPECTRAL OF PLL WITHOUT 94 GHZ SOURCE.....	56
FIGURE 39 JTFA RESULTS WITHOUT 94 GHZ SOURCE.....	57
FIGURE 40 VCO SPECTRAL RESPONSE WITH 94 GHZ.....	57
FIGURE 41 PLL FREQUENCY RESPONSE WITHOUT RF.....	58
FIGURE 42 95 GHZ PRF = 27 Hz 50% DUTY CYCLE.....	58
FIGURE 43 95 GHZ PRF = 50 Hz 50% DUTY CYCLE.....	59
FIGURE 44 95 GHZ PRF = 100 Hz 50% DUTY CYCLE.....	59
FIGURE 45 95 GHZ PRF = 100 Hz 50% DUTY CYCLE.....	60
FIGURE 46 PLL LOW PASS FILTER RESPONSE.....	60
FIGURE 47 MOTOROLA AND PLL CONTROLLER CIRCUIT.....	61
FIGURE 48 MOTOROLA AND PLL CONTROLLER.....	62

Intentional Left Blank

Introduction

The U.S., the Soviet Union, and other countries have studied high power microwaves (HPM) and their effects on electronics for decades. HPM systems generate high power radio frequency (RF) energy in the power range of kilowatts to gigawatts. The HPM system deposits RF energy into a target system in an effort to cause the target system to experience either temporary upset (latch-up or reset) or failure (electronics damage). The required RF power needed to cause either effect is high compared to available systems. Members of the HPM community have suggested a new low-power threshold mechanism to cause system failure. The new mechanism, based on nonlinear dynamics, requires one to expand their way of thinking about how electronic circuits operate. In this effort, we developed models, performed simulations, and conducted key experiments to determine the validity of the claim of lower-power thresholds. Our goal was to confirm or refute the claims made and to fully understand the effect of nonlinear dynamics in circuits. We spent a significant portion of this effort studying a fundamental circuit called the Linsay circuit. The Linsay circuit (Figure 1) is composed of an inductor, a series resistance, a diode with inherent nonlinear capacitance, and a source to stimulate the circuit. Dr. Linsay was the first to study the behavior of this circuit. Our early simulation results of this system suggested that upset was obtainable with low induced voltages. Understanding this new mechanism of upset is important to the long-term viability of the nuclear weapon stockpile (new designs and retrofits). We seek to fully understand this threat so that we can perform system-specific assessments required by a customer.

The first part of the report describes the theory of nonlinear dynamics. The second part of this report describes modeling and testing we performed on the Linsay circuit. The goal of this effort was to understand the behavior of a single PN junction exposed to voltage sufficient to cause the junction to behave in a chaotic manner. The third part of this report addresses measurements made on a phased-locked-loop (PLL). We chose to study a PLL since this circuit is in many systems including control systems

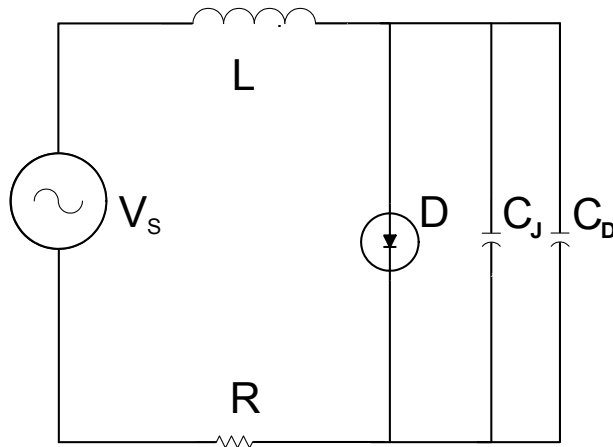


Figure 1 The Linsay Circuit

The Linsay circuit is composed of an inductor, a series resistance, a diode with inherent nonlinear capacitance, and a source to stimulate the circuit.

Nonlinear Dynamics Theory

History

Today the study of nonlinear dynamics is one of the most exciting and fastest growing branches of the mathematical sciences. Nonlinear dynamics is having an increasingly important impact on a variety of applied sciences ranging from the study of turbulence, the behavior of weather, and the study of mechanical and electrical systems. Previously, scientists--having limited computing power--would breakup the object of their study into linear pieces; hence, the term piecewise linear. For many years, mathematicians knew about complicated systems of equations but were unable to solve these systems because most problems had no known analytical solutions. Studying celestial behavior, Henry Poincaré found (~1889) a system of equations that was the first known mathematical expression for a chaotic system. Even given the complications, mathematicians performed pain-staking hand calculations to obtain approximate solutions. In 1963, Edward Lorenz encountered a chaotic system while analyzing a model he derived to study the behavior of the weather. Lorenz found that his model yielded very different solutions with extremely small variations in initial conditions. Sensitivity to initial conditions is a key indicator of a chaotic system as we will discuss later in this paper. Since Lorenz's discovery, mathematicians have intensified their efforts to understand nonlinear dynamical

systems. Only recently (since Lorenz), have scientists started to use this study of mathematics to study practical physical systems.

Researcher delay in using nonlinear dynamics theory in the applied sciences is rooted in the fact that solutions to chaotic system necessitate numerical solutions since no one has yet to find analytical solutions to these systems. Today computers have much more power than they did just a few years ago and researchers are taking advantage of the enhanced computer power to study nonlinear systems in detail. In the case of our study of electronic systems, one tool we used was a commercial product widely used throughout the industry of electronic design known as SPICE. The University of Berkeley, California introduced Spice in May of 1972; the name Spice is an acronym and stands for ‘Simulation Program with Integrated Circuit Emphasis’; notice the emphases on integrated circuits. Analog integrated circuits normally operate in a low power linear range. Nonlinear circuit behavior occurs at power levels well above the power normally used for analog integrated circuit design. This fact suggests that SPICE may not be the proper tool for studying nonlinear dynamics. Researchers studying the nonlinear dynamics behavior of electronic circuits base their model on SPICE in every detail. These models do produce chaotic behavior, but the simulation results differ significantly from experimental results. We find in this study that the SPICE diode model does not produce simulation results that agree with measurements when subjected to high drive signals. In this paper, we will describe the nature of the model inaccuracies and how the models we develop provide better performance than the models normally used in SPICE simulators.

Metrics of Chaos

Devaney¹ gives a strict mathematical definition of chaos in his book, but chaos centers on the issue of the difficulty to make accurate long-term predictions of system behavior. In linear circuits, small variations in initial conditions cause small changes in the circuits long-term behavior. A chaotic system is deterministic, since given the system and the exact initial conditions the system behavior is repeatable. However, the behavior of two identical systems with different initial conditions—differing by the smallest amount—will diverge exponentially. The Lyapunov number quantifies the rate of divergent behavior between the two systems offering a measure of the quantity of chaos. People often equate the property of the Lyapunov

number and the magnitude of chaos. We will describe the details of Lyapunov numbers later in this paper.

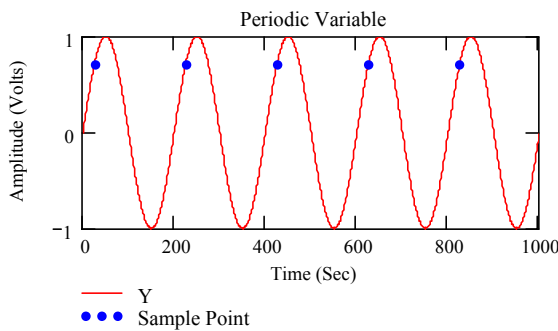
In order to understand chaotic behavior better, we must define some mathematical terms. First, consider a system with a state variable we characterize as follows. The variable has a supremum and an infimum. In simpler terms, the supremum and infimum bound the chaotic variable. Without loss of generality, let's call this variable y . Further, assume that the value y is a function of time $y=f(t)$. We now define a periodic function. A function is periodic if it meets the following conditions: $y=f(t)=f(nT+t)$. What this equation states is that the function f will equal y at a particular time (t), and the function f will again equal y some time later ($t+nT$). Where, T is the time between each occurrence of $y=f(t)$ and n is a non-zero integer value. Figure 2(a) shows a sine function (in red) and a periodic sample (in blue), of the same sine function, once every cycle at a fixed time. We can define much more complicated periodic functions, but the idea is--the value of the function at time intervals equal to the period are the same.

Researchers often plot this function against the same function shifted in time. In this example, Figure 2(b) shows a plot of $Y(t)=\sin(t)$ vs. $Y(t)=\sin\left(t+\frac{\pi}{2}\right)$. The result shown in Figure 2(b) is a circle. A more complicated variable would yield a more complicated result, and for this example, if the phase-shift were a different value, a more general shape—an ellipse—would appear. Often before a system goes into chaos, the behavior goes into a state of period doubling as shown in Figure 2(c) and 2(d). When period doubling occurs $y=f(t)=f(2n\Delta t+t)$. This equation states the function now repeats on twice the time scale as the original function. When this occurs, the phase space plot of the period doubled function produces two loops. Period tripling and higher levels of period increase the number of loops.

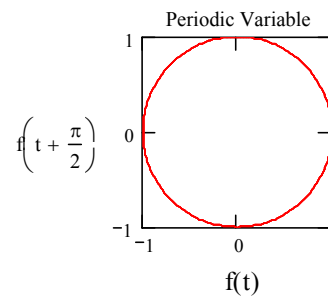
When a system is in a chaotic state, many orbits appear creating a visual appearance of smearing together of the orbits. The chaotic behavior confines the orbits to a region (or regions), but every orbit does not exactly overlay any other orbit. Figure 3 shows the phase space plot of a Lorenz system where the function is chaotic.

Dynamical System

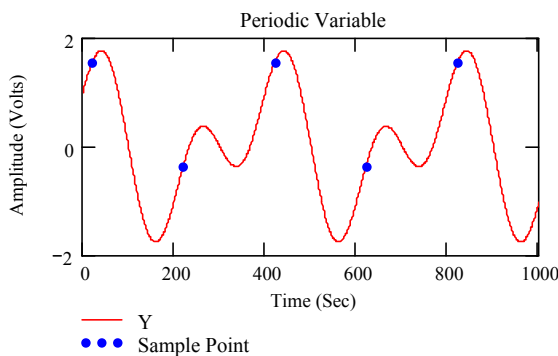
A dynamical system describes how one state develops into another state over time. Technically, a dynamical system is a smooth action of real numbers or integers on another object (usually a manifold). When real numbers are acting, the system is a continuous dynamical system, and when the integers are acting, the system is a discrete dynamical system. If f is any continuous function, then, $x_{n+1} = f(x_n)$, describes the evolution of x —called a flow. This equation, viewed as a difference equation, is expressed as $x_{n+1} - x_n = f(x_n) - x_n$. Therefore, defining $g(x_n) = f(x_n) - x_n$ gives $x_{n+1} - x_n = g(x_n) * 1$, which is read “as n changes by 1 unit, x changes by $g(x_n)$ ”—called a map. $g(x_n)$ is the discrete equivalent of the differential equation $x'(n) = g(x(n))$. A trajectory describes a path (or sequence of points) that a progression of values takes over time—described by either a flow (continuous) or a map (discrete).



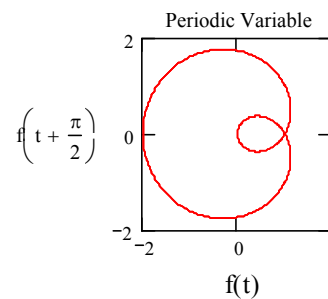
(a) Periodic variable sampled once every cycle.



(b) Phase space plot.



(c) Period-doubled variable sampled once every cycle.



(d) Phase space plot of period-doubled variable.

Figure 2 Periodic Variable

In (a) a periodic signal is sampled at the fundamental frequency producing a DC voltage dependent on peak voltage and phase where the sample occurs. In (b) a circle is created by plotting the signal in (a) against itself delayed by 90° . In (c), the signal is composed of two frequency components. Hence, in (d) two loops are formed that indicate a period doubling is a result of the subharmonic. When a circuit is chaotic, subharmonics are created and a phase plot can show the existence of a subharmonic as illustrated here.

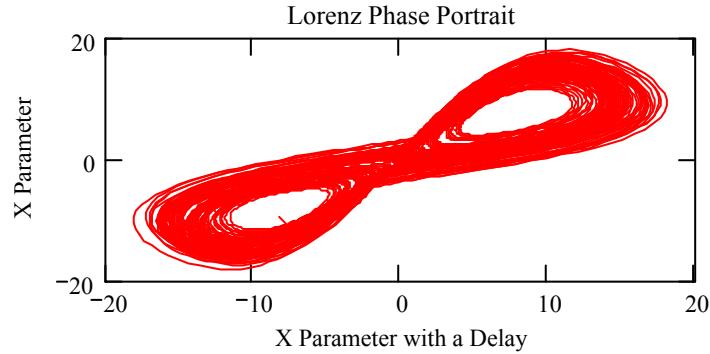


Figure 3 Phase Space Plot

This Lorenz system illustrates chaotic behavior. Although the trajectory is confined to a region, the trajectory never repeats its path.

Reconstruction

Real dynamical systems evolve in time over a multidimensional phase space; however, rarely is the phase space of a system under study known. In many cases, the data under investigation is a sequence of points—each point representing a scalar value associated with a time. This data set is a transformation of the real dynamical system. The analyst uses these data to reconstruct a system that contains the pertinent parameters of the measured system. In 1981, Taken² proved that some property values (i.e. Lyapunov numbers, correlation dimensions, etc.) of the dynamical system are invariant to smooth transformations. Hence, with a properly reconstructed surrogate system we can gain insight into the real system.

One approach to reconstruct a system is to use delayed elements of the measured data. Suppose we have a dynamical system $\mathbf{x}(n) \rightarrow F(\mathbf{x}(n)) = \mathbf{x}(n+1)$ where $\mathbf{x}(t)$ phase space is multidimensional. Taken's theorem tells us if we are able to observe a single scalar quantity $\mathbf{h}(\bullet)$, of some vector function of the dynamical variable $\mathbf{g}(\mathbf{x}(n))$, then the geometric structure of the multivariate dynamics can be unfolded from this set of scalar measurements $\mathbf{h}(\mathbf{g}(\mathbf{x}(t)))$ into the space from new vectors with components consisting of $\mathbf{h}(\bullet)$ applied to powers of $\mathbf{g}(\mathbf{x}(t))$. These vectors $\mathbf{x}_n = (x_{n-(m-1)}, x_{n-(m-2)}, x_{n-(m-3)}, \dots, x_{n-v}, x_n)$ define motion in a d-dimensional Euclidian space. With general conditions of smoothness on the functions $\mathbf{h}(\bullet)$ and $\mathbf{g}(\mathbf{x}(t))$, it has been shown³ that if the dimension is large enough, then many important properties of the unknown multivariate signal $\mathbf{x}(n)$ at the source of the observed chaos are reproduced without

ambiguity in the new space of vectors $\mathbf{s}(n)$. Taken showed, that the sequential order of the points $\mathbf{s}(n) \rightarrow \mathbf{s}(n+1)$ follows the unknown dynamics $\mathbf{x}(n) \rightarrow \mathbf{x}(n+1)$. The deterministic behavior of the underlying source of observations, $\mathbf{x}(n) \rightarrow \mathbf{x}(n+1)$, assures the deterministic behavior of the substitute representation of this dynamical $\mathbf{s}(n) \rightarrow \mathbf{s}(n+1)$; the dimension of the reconstructed space does not need to be the same as the original space. Care must be taken to ensure that the reconstructed space does not falsely project vectors close to one another due to the construction. False neighbors can arise from projections of higher dimensional systems to lower dimensional systems. A delay reconstruction in m dimension forms a vectors, given by $\mathbf{s}_n = (s_{n-(m-1)v}, s_{n-(m-2)v}, s_{n-(m-3)v}, \dots, s_{n-v}, s_n)$, where \mathbf{x}_n is the sequence from the data. The time difference in number of samples, v , is referred to as the lag or delay time. The geometrical object created from this process is clearly different from the original trajectory x_n . An important question is: in what sense is the artificial object equivalent to the original? It turns out that if the dimension of \mathbf{x}_n is sufficiently large, then many properties formed by \mathbf{x}_n are equivalent to the properties of the unknown space, x_n , in which the original system lives—provided the dimension of m , the delay coordinate space, is sufficiently large. Therefore, one can estimate the dynamical properties of the original system from the reconstructed system. There are other approaches to characterize the nonlinear behavior, but this is the approach we used in our study.

Lyapunov Numbers

Exponential growth of infinitesimal perturbations and global folding mechanisms to guarantee boundedness of the solutions are major components of chaos. The exponential nature characterizes a spectrum of Lyapunov exponents⁴. Assuming a local decomposition of the phase space into directions with different stretching or contraction rates, the spectrum of exponents is the average of these local rates over the whole invariant set, and thus consists of as many exponents as there are space directions. The most prominent problem in time series analysis is that the physical phase space is unknown, and the observed spectrum is from some an embedded (reconstructed) space. Consequently, the number of exponents depends on the reconstruction, not the actual dynamics, and the number could exceed (or be less than) the true phase space. Techniques exist to either avoid additional exponents (called spurious⁵) or to identify extra

exponents. Lyapunov exponents are invariant under smooth transformations and are thus independent of the embedding procedure.

An explicit construction of a model is not essential to establish the maximal Lyapunov exponent. A reliable characterization requires that the independence of embedding parameters and the exponential law for the growth of distances are explicitly checked^{6,7}. If one considers a time series as a trajectory in the embedding space, and that $s_{n'}$ is a close return to a previously visited point s_n , then one can consider the distance $\Delta_0 = s_n - s_{n'}$ as a small perturbation, which grow exponentially in time if the system is chaotic. Later values of the trajectory of s define the later perturbations $\Delta_l = s_{n+l} - s_{n'+l}$. If $|\Delta_l| \approx \Delta_0 e^{\lambda l}$, then λ is the maximal Lyapunov exponent. In practice, there are fluctuations for many reasons discussed in detail by Kantz and Schreiber⁸. Understanding this, one derives a robust consistent and unbiased estimator for the maximal Lyapunov exponent.

$$S(\varepsilon, m, t) = \left\langle \ln \left(\frac{1}{|U_n|} \sum_{s_{n'} \in U_n} |s_{n+t} - s_{n'+t}| \right) \right\rangle_n .$$

If $S(\varepsilon, m, t)$ exhibits a linear increase with identical slope for all m larger than some m_0 and for a reasonable range of ε , then this slope can be taken as an estimate of the maximal Lyapunov exponent.

Fractal numbers

Another metric of chaotic behavior is the fractal number. Benoit Mandelbrot, the discoverer of the Mandelbrot set, coined the term "fractal" in 1975 from the Latin fractus or "to break". Mandelbrot defines a fractal as a set which the Hausdorff-Besicovich dimension strictly exceeds the topological dimension. However, Mandelbrot was not satisfied with this definition since it excludes sets one would consider fractals.

Dimensions characterize a set or an invariant measure whose support is the set, whereas any data set contains only a finite number of points representing the set of the measure. By definition, the dimension of a finite set of points is zero. We extrapolate, from finite length scales, where the statistics we apply is insensitive to the finiteness of the number of data, to the infinitesimal scale, where the concept of dimensions is defined. This extrapolation can fail for many reasons. A common type of fractal dimension is the Hausdorff-Besicovich Dimension,

although there are several different ways of computing fractal dimension. One can calculate the fractal dimension by taking the limit of the quotient of the log change in object size and the log change in measurement scale, as the measurement scale approaches zero. The differences come in the exactly meanings of "object size" and "measurement scale" and how to average the many different parts of a geometrical object. Fractal dimensions quantify the static geometry of an object.

For example, consider a straight line. Now increase the line by a factor of two. The line is now twice as long as before. Since, $\frac{\log(2)}{\log(2)} = 1$, the dimension is 1. Now consider a square and blow up the square by a factor of two on each side. The square is now 4 times as large as before. $\frac{\log(4)}{\log(2)} = 2$, corresponding to dimension 2 for the square. Now consider a snowflake curve (Figure 4) formed by repeatedly replacing each straight segment with four segments that are one-third the length of the original segment, $\frac{\log(4)}{\log(3)} = 1.26185\dots$. Since the dimension 1.261 is larger than the dimension 1 of the lines making up the curve, the snowflake curve is a fractal. There are many other examples in the literature.

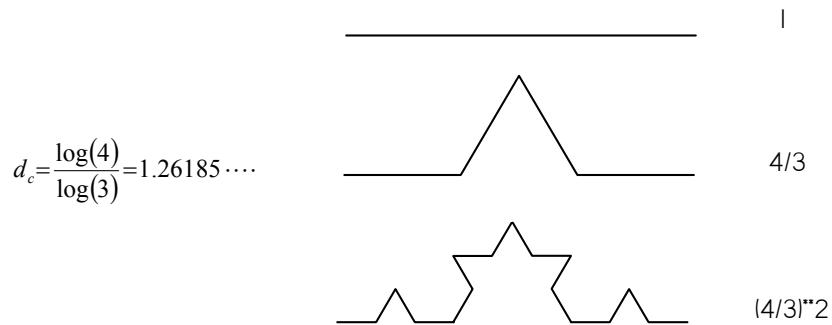


Figure 4 The Koch Snowflake

This figure shows the fractal nature of segmenting a line. The total length of the line increases by a factor of 1.26/division when increasing the number of segments.

Poincaré Maps

Although researchers have developed several analytical numerical techniques to characterize the chaotic behavior of data, the first process a researcher usually performs is to create a visual representation of the data set. One such visualization tool is the Poincaré map. To create such a map, one forms a suitable orientated surface in phase space.

Researchers use Poincaré maps (Figure 5) to distinguish between various qualitative states of motion such as periodic, quasi-periodic, or chaotic. One creates a Poincaré map by stroboscopically measuring the dynamic variables at some particular phase of the forcing motion. In an n -state variable problem, one can obtain a Poincaré section by measuring the $n-1$ variables when the n th variable reaches some particular value or when the phase space trajectory crosses some arbitrary plane in phase space. Another common plane used to create a Poincaré map is to plot maximum or minimum values. In fact, we used this method to describe some of the experimental results.

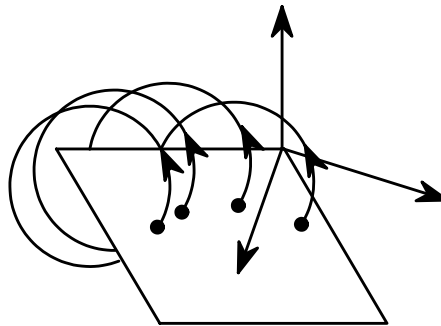


Figure 5 Poincaré Map

Samples of the trajectory in a phase plane are the elements of a Poincaré Map. The phase plane is defined in a way that provides a visual pattern.

Bifurcation

In nonlinear dynamical study, bifurcation plots help visualize any sudden changes in the behavior of a system as some parameter is varied. Bifurcation refers to splitting the system behavior into two regions: one region above and the other region below the particular parameter value at which the change occurred. Bifurcation plots are derived from Poincaré maps. Figure 6 shows an example bifurcation plot from a Linsay circuit. The bifurcation plot measures motion of a parameter as function of a system parameter such as forcing amplitude or damping constant. It is very easy to observe period doubling and sub-harmonic bifurcations from Figure 6.

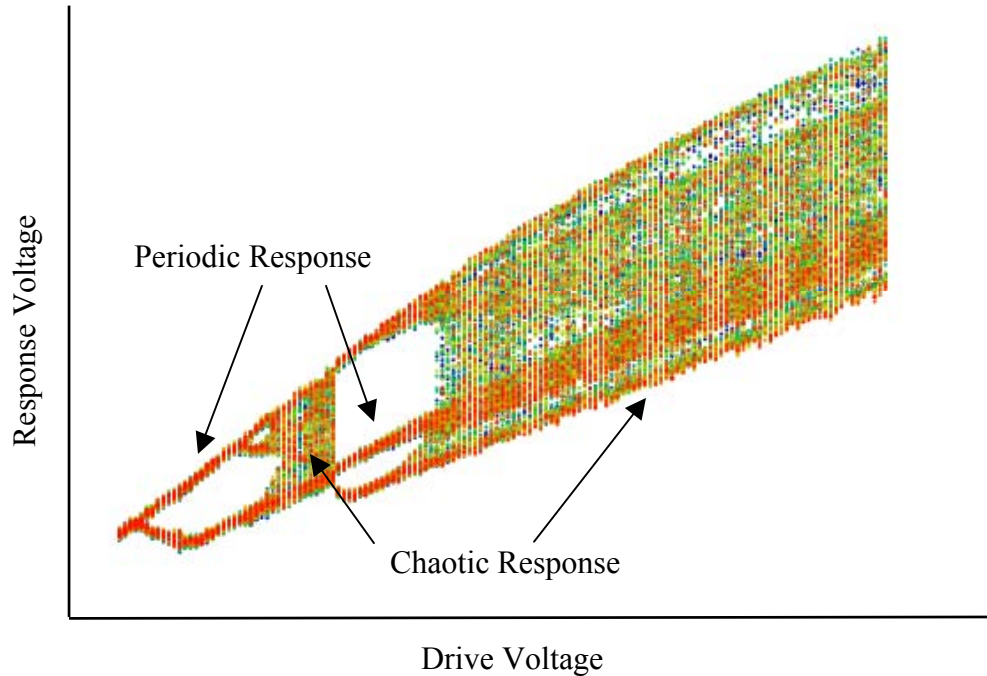


Figure 6 Bifurcation Plot

The ordinate in this graph is the voltage of the system sampled at a fixed period. The abscissa is the voltage applied to the circuit. At different applied voltages, the response is either periodic or chaotic.

Linsay Circuit

As mentioned in the introduction, we exerted a significant effort studying what on the surface appeared to be a simple problem. With the improvement in computing power and the need to model circuit behavior with greater precision, the nonlinear effects of circuit has become very important. In addition, every integrated circuit has as part of its design a protective circuit. These projective circuits use some variation of semiconductor junctions that can interact with parasitic components, present in every real system. Hence, the protective circuit can behave as a Linsay circuit.

Researchers refer to the first electronic circuit shown to exhibit chaotic circuit as the Linsay circuit and is shown in Figure 1. As one can see from the circuit model, three storage components and one dissipative component exists. The interactions of these components and the fact that the characteristics of C_j and C_d are nonlinear cause the circuit to behave chaotically. This document will explain—in a later section—how this circuit exhibits nonlinear behavior.

Theory and Simulations

We used the following system of differential equations to solve the Linsay circuit. Figure 7 is a reprint Figure 1 for the reader's convenience.

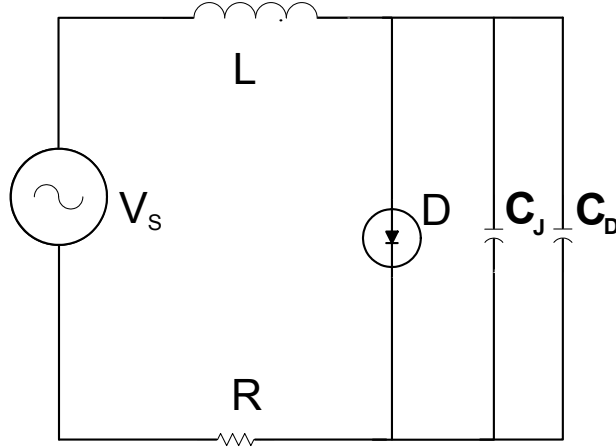


Figure 7 Linsay circuit

The Linsay circuit is composed of an inductor, a series resistance, a diode with inherent nonlinear capacitance, and a source to stimulate the circuit. This is the basic circuit description used in modeling.

$$V_d(t) = \frac{1}{C_j(t) + C_d(t)} \dot{Q}_d(t) \quad (1)$$

$$\dot{C}_d(t) = \frac{\left(\dot{Q}_d(t) \right)}{n * V_T}, \quad V_T = \frac{k * T}{q} \quad (2)$$

$$\frac{d}{dQ_j} C_j(Q_j) = \left\{ \begin{array}{l} \left(\frac{T_d}{T_m} \right) \frac{m}{\phi_0} \frac{1}{1 - \frac{V_d(t)}{\phi_0}} \quad \text{if } V_d(t) < F_c * \phi_0 \\ \left(\frac{T_d}{T_m} \right) \frac{m}{\phi_0} \frac{1}{1 - F_c} \frac{1 - \frac{V_d(t)}{\phi_0}}{1 - F_c} \quad \text{if } F_c * \phi_0 < V_d(t) < \phi_0 * (2 - F_c) \\ \left(\frac{T_d}{T_m} \right) \frac{m}{\phi_0} \frac{1}{1 - F_c} e^{\frac{m \left(2 - F_c - \frac{V_d(t)}{\phi_0} \right)}{1 - F_c}} \quad \text{if } \phi_0 * (2 - F_c) < V_d(t) \end{array} \right. \quad (3)$$

$$\dot{C}_j(t) = \frac{d}{dQ_j} C_j(Q_j) * \frac{d}{dV_d} Q_j(V_d) * \dot{V}_d(t) \quad (4)$$

$$I_t \dot{(t)} = \frac{1}{L} (V_s - R * I_t(t) - V_d(t)) \quad (5)$$

$$\dot{I}_d(t) = \left(\frac{I_s * e^{\frac{V_d(t)}{n * V_T}}}{n * V_T} \right) * \left(\dot{V}_d(t) \right) \quad (6)$$

$$V_s = A * \sin(\omega t) \quad (7)$$

$$\dot{Q}_t(t) = I_t(t) - \left(\frac{Q(t)}{T_d} \right) \quad (8)$$

$$\dot{Q}_d(t) = T_d \left(\dot{I}_d(t) \right) \quad (9)$$

$$\dot{Q}_j(t) = C_j \left(\dot{V}_d(t) \right) \quad (10)$$

$$C_j(V_d) = \frac{C_{j0}}{\left(1 - \frac{V_d}{\phi_0} \right)^m} \quad (11)$$

To correct for inaccurate SPICE results, we used an expression for dynamic diffusion capacitance found in Millman and Halkias⁹. The diffusion capacitance and the conductance of the diode are frequency dependent.

$$C_d = g_0 \left(\frac{\tau_p}{2\omega} \right)^{\frac{1}{2}} \quad (12)$$

$$g = g_0 \left(\frac{\omega \tau_p}{2} \right)^{\frac{1}{2}} \quad (13)$$

g_0 is the low frequency conductance. ω is the radian frequency. τ_p is the recombination life time. The model of a diode in Micro-Cap^{*} does not allow the user to change the value of C_d directly. To accommodate the frequency dependence of the diffusion capacitance, we scaled the value of the transient time. In Micro-Cap, the expression for diffusion capacitance is

* Micro-Cap is a commercially available SPICE simulator.

$$C_d = g_0 * TT \quad (14)$$

TT is the transit time. Sandia National Laboratories Group 1734 measured the transit time of all the diodes that we tested. For a fixed frequency the transit time of the diode was scaled using the scale factor in equation 12. One finds the charge on a linear capacitor by taking the product of C and V . Since both C_j and C_d are voltage dependent, the charge on the capacitors is expressed in general terms by equation 15 and the current is expressed by equation 16. In this case, this approach leads to an inaccurate result. Since nonlinear systems are exquisitely dependent on initial conditions, any error in the charge however small, places the solution of the nonlinear system on a different trajectory.

$$Q = \int C(V) * dV \quad (15)$$

$$I = C(V) * \frac{dV}{dt} \quad (16)$$

Simulation Results

We ran several simulations to validate the model developed under this effort. We used Fortran and Micro-Cap to perform the simulations. The results from both software packages were comparable. Finding that the results were equivalent is important. The Linsay circuit is simple; using SPICE-based software to simulate circuits that are more complicated reduces the modeling difficulty and time of model development. We record the results of our simulations here and compare these results to our experimental results. We give additional experimental results in the following section. Figure 8 shows very good agreement between the simulated (red solid) and measured (blue dashed) time domain responses. Note that the simulation does not overlay the measurement exactly since the nature of a chaotic signal guarantees a difference between the two results.

The time domain and frequency domain results show that the linear properties of the experimental and simulated results are in very good agreement. In addition, the Lyapunov number, an indication of the rate at which information is lost in the signal, is similar for both the simulation and measured results. As stated in the theory section of this paper, the Lyapunov number is a measure of the rate of divergence between two points (two waveform) with increasing time. Hence, two waveforms with ever so slightly different values, at a given time, will have vastly different values at a later time as shown in Figure 9.

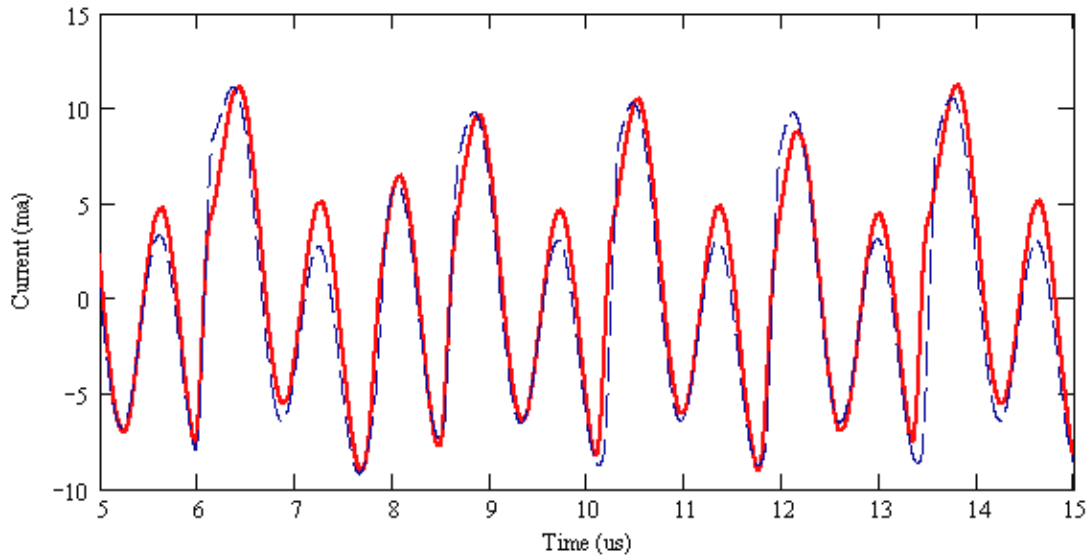


Figure 8 Time Series Results Early in the Series

The Red solid line shows the experimental results. The blue dashed line shows the simulation results. This figure illustrates the close comparison of simulation results and measured results.

Figure 10 shows the spectral response of the time domain waveform captured by the experiment (red solid) and the simulation (blue dotted). The main feature of a chaotic response is the sub-harmonic content. The spectrum of both the simulation results and the measured results below the fundamental of 1.22 MHz are in very good agreement. In addition, the spectral content above the fundamental is also in very good agreement.

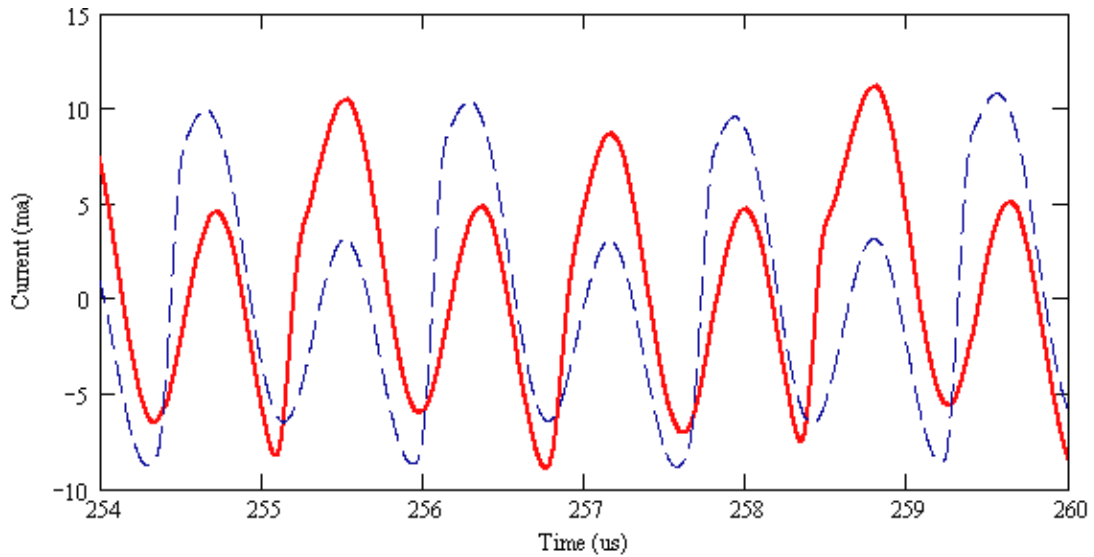


Figure 9 Time Series Results Late in the Series

The red solid line shows the experimental results. The blue dashed line shows the simulation results. This figure illustrates the difference in experimental results and measured results later in the time series. Due to the nature of chaotic systems, the results necessarily diverge. Compare these results to those shown in Figure 8 above.

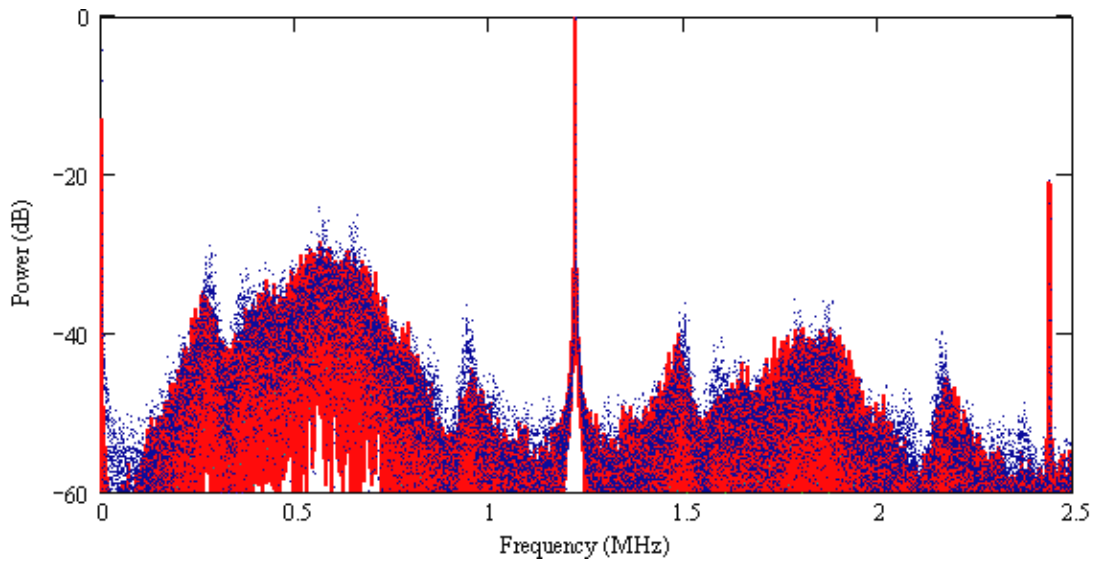


Figure 10 Spectral response

The spectral response of time domain waveform shown in Figure 9 above. The red solid line shows the experimental results. Blue dotted line shows the simulation results. This graph shows very good agreement between the experimental results and the measured results.

Figure 11 shows the measured and simulated Lyapunov exponents. The slope of the leading edge of the line is the Lyapunov number. The Lyapunov number represents the average rate at which two points diverge. It is important to note that even though the points diverge from each other, the trajectories are bounded and any two waveforms can also become arbitrarily close at a later time. The Lyapunov number from the measured results is $6.5 \cdot 10^{-4} / \text{sec}$. The Lyapunov number from the simulated results is $5.4 \cdot 10^{-4} / \text{sec}$.

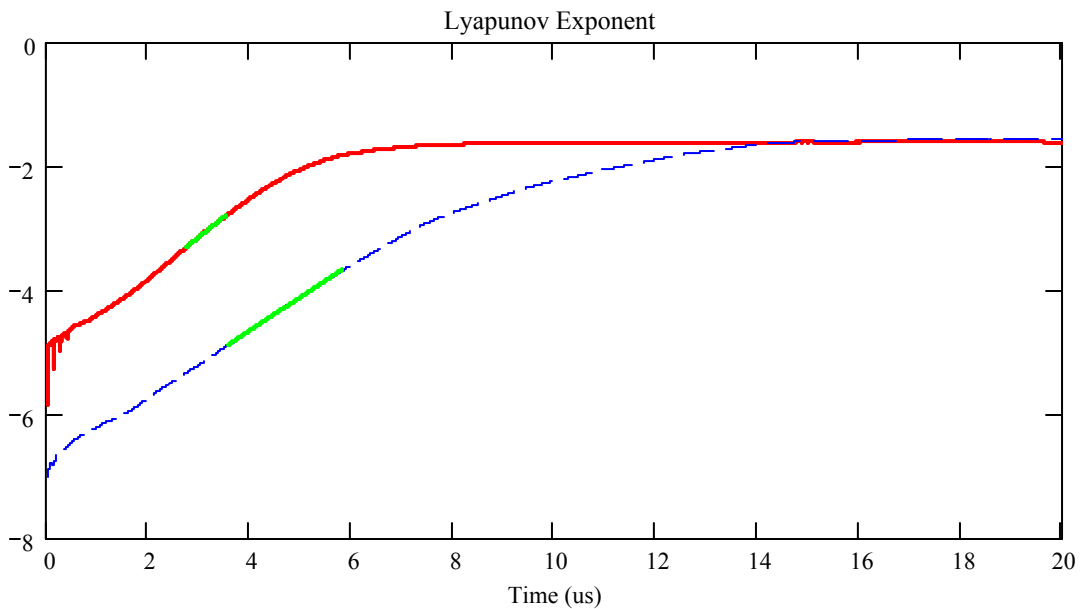


Figure 11 Lyapunov Results

The red solid line shows the experimental results $6.5 \cdot 10^{-4} / \text{sec}$. The blue dashed line shows the simulation results $5.4 \cdot 10^{-4} / \text{sec}$. This is very close agreement between the experimental result and the measured results. The Lyapunov number is a measure of the rate that trajectories diverge. Diverging in the sense that two points initially very close on two trajectories will diverge from each other exponentially and eventually will be arbitrarily far way from each other.

Experimental Results

Refer to Figure 12 for the following discussion. A diode dynamically switching from forward conduction (on state) to reverse non-conducting (off state) is commonly said to undergo a turn-off transient. The time of the turn-off transient is the reverse recovery time (t_{rr}). The measured reverse recovery time of the diode depends on the properties of the circuit the diode is in, including: the waveform used for the measurement, forward current, and the reverse current. The storage delay (t_{sd}) is the time the diode maintains full reverse current. During t_{sd} , the diode behaves as an ideal voltage source, since the diode voltage is constant and current is supplied by the diode. The reverse recovery time, t_{rr} , is the time the diode current initially reverses until the current reduces to 10% of the magnitude of its maximum value. Typically, the t_{rr} setup includes a pulse generator (with an internal impedance of 50Ω) connected in series with the diode and a 50Ω termination. The input impedance of the oscilloscope serves as the 50Ω load.

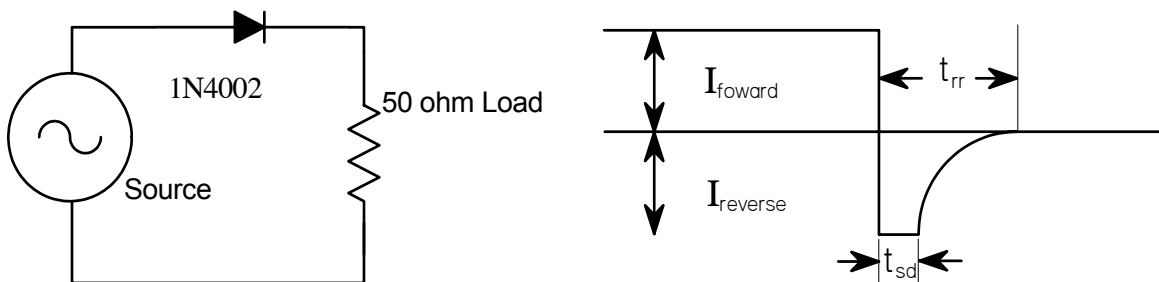


Figure 12 Reverse Recovery

Test Setup and Waveform. The setup on the left shows the circuit used to measure reverse recovery. On the right is a text book result of reverse recovery. During this test, the diode is forward biased then reverse biased where the current drops from $I_{forward}$ to $I_{reverse}$. The time that $I_{reverse}$ remains at its maximum is defined as the storage delay time. The reverse recovery time is defined as the time needed for the reverse current to drop to zero.

Reverse recovery occurs due to excess minority carrier buildup in the pn junction during forward bias. The excess minority carriers is what allows the diode to conduct in the forward direction. When the diode bias reverses, the excess minority carriers recombine and the pn junction losses its excess charge. The time needed to deplete the excess minority carriers is the

recovery time. When the excess charge depletes, the diode current establishes a static reverse current value. Reverse recovery time of a diode depends on the recombination time of the

minority carries (τ_p) in the n material, where $t_{rr} = \tau_p \left(\text{erf}^{-1} \left(\frac{I_{forward}}{I_{forward} + I_{reverse}} \right) \right)^2$, $I_{forward}$, and

$I_{reverse}$ are the forward and reverse currents of the diode and erf is the error function. The

transient time (TT) used for circuit simulations is $TT = \left(\frac{1}{t_{rr}} - \frac{1}{\tau_p} \right)^{-1}$. We determined the

transient time of each diode by adjusting the SPICE model transient time; performed a simulation and compared the simulation result to measured result. Since the reverse recovery time depends on external properties, we used the standard test setup to measure reverse recovery and performed the simulation with the same setup. We studied the nonlinear behaviors of six diodes. In addition to transit time, personnel from 1734 measured the diode parameters shown in the Table 1.

The reverse recovery times of diodes range from sharp recovery edges like in standard rectifier diodes, a soft turn off like those used in IGBTs, to Schottly diodes having little or no time associated to their recovery. The manufacturing process and diode tolerances determine reverse recovery. Standard diodes like the 1N4002 and 1N4005 typically have t_{rr} times of a few microseconds.

Table 1 SPICE Parameters for Six Different Test Diodes

Name	Diode 3	Diode 6	Diode 7	Diode 8	Diode 10	Diode 11
Type	1N4002	1N4002	1N4005	1N4005	1N4002	1N4002
I_s (amps)	0.8211n	0.1729n	2.278n	5.308n	0.1613n	2.684n
N	1.599	1.489	1.699	1.786	1.47	1.712
BV (Volts)	100	100	100	100	100	100
IBV (Volts)	0.001	0.001	0.001	0.001	0.001	0.001
RS (ohms)	0.02079	0.02615	0.03406	0.01895	0.0305	0.02223
C_{jo} (Farad)	44.54p	44.09p	17.68p	20.19p	47.72p	42.11p
V_j (Volts)	0.4027	0.4009	0.2046	0.2376	0.4263	0.4085
M	0.3624	0.3688	0.3092	0.3137	0.3730	0.3689
FC	0.5	0.5	0.5	0.5	0.5	0.5
TT (sec)	7.3 μ	8.0 μ	10.2 μ	8.8 μ	9.0 μ	8.72 μ
EG (eV)	1.11	1.11	1.11	1.11	1.11	42.11p
XTI	3	3	Default	Default	Default	Default

Diodes 3, 6, 10, & 11 (1N4002) had similar reverse recoveries with sharp rising edges while the recovery profiles for Diode 7 & 8 (1N4005) were more gradual. See Figure 13. The simulations do not show differences in recovery shape.

The amount of charge Q in the depletion region of the pn junction of a diode is dependant on several variables; doping concentrations, the physical area, as well as, the bias voltage. The effective capacitance of the diode is the sum of junction and diffusion capacitance plus any parasitics. The effective capacitance is a function of bias voltage and drive frequency. The effective capacitance of the diode is a major contributor to the reverse recovery time.

We measured the capacitance of Diode 11 with an impedance analyzer, the value C_{j0} ranged from 80pF to 42pF for a frequency drive of 50Hz to 1MHz. C_{j0} is the equivalent capacitance of the diode at zero bias. Shown in Figure 15 is a family of capacitance curves. The parameter is frequency and the independent variable is bias voltage. The simulation results compares well with the measurement at 1 MHz until reaching the forward bias region. In the forward bias region, the simulation capacitance is much greater than the measured capacitance. The simulations do not predict a frequency dependence on capacitance, but the measurements clearly show dependence.

When the diode is fully conducting, the capacitance peaks and the diode is fully charged. As the voltage across the diode switches from forward to reverse bias, the excess charge established by minority carriers dissipates and the charge in the pn junction eventually establishes a new equilibrium value. When the period of the reverse bias is insufficient to cause the diode to deplete the stored charge the forward bias will increase the charge on the diode to its maximum value in a shorter period. The diode will develop a charge “memory” apparent in its recovery time. The result is that the I-V characteristics of the diode changes when the period of the drive voltage is less than reverse recovery time.

Given Diode 11’s measured reverse recovery time of 8.0 μ s, 62.5 kHz ($2 \cdot 8.0 \mu$ s) is the maximum frequency that the diode is able to switch polarities. At faster frequencies, the diode begins to exhibit a charge hysteresis. Figure 14 shows reverse recoveries of Diode 11 after a single pulse transition and after the eighth pulse in a pulse train for the drive frequencies of 250 kHz, 500 kHz, and 1 MHz. These results show no difference in reverse recovery between a single-pulse and last pulse of an eight-pulse transition for either the simulation or measured results at 250 kHz. At 500 kHz, the measurements indicate a difference between the single-pulse

and the pulse train. However, the simulation shows no difference. At 1MHz, both the simulation and measured results show that the reverse recovery time of the pulse train is greater than the single-pulse. Though the simulations and experimental results indicate that a pulse train increases the recovery time, the simulation does not predict the experimental results.

Figure 15 shows the effective capacitance across the diode as a function of diode bias voltage. We measured experimental results at different drive frequencies. For all cases, when the diode is in full forward conduction, the capacitance is at a maximum and the diode is fully charged. Figure 15 also shows simulated for 1 MHz. Simulation results were not frequency dependent.

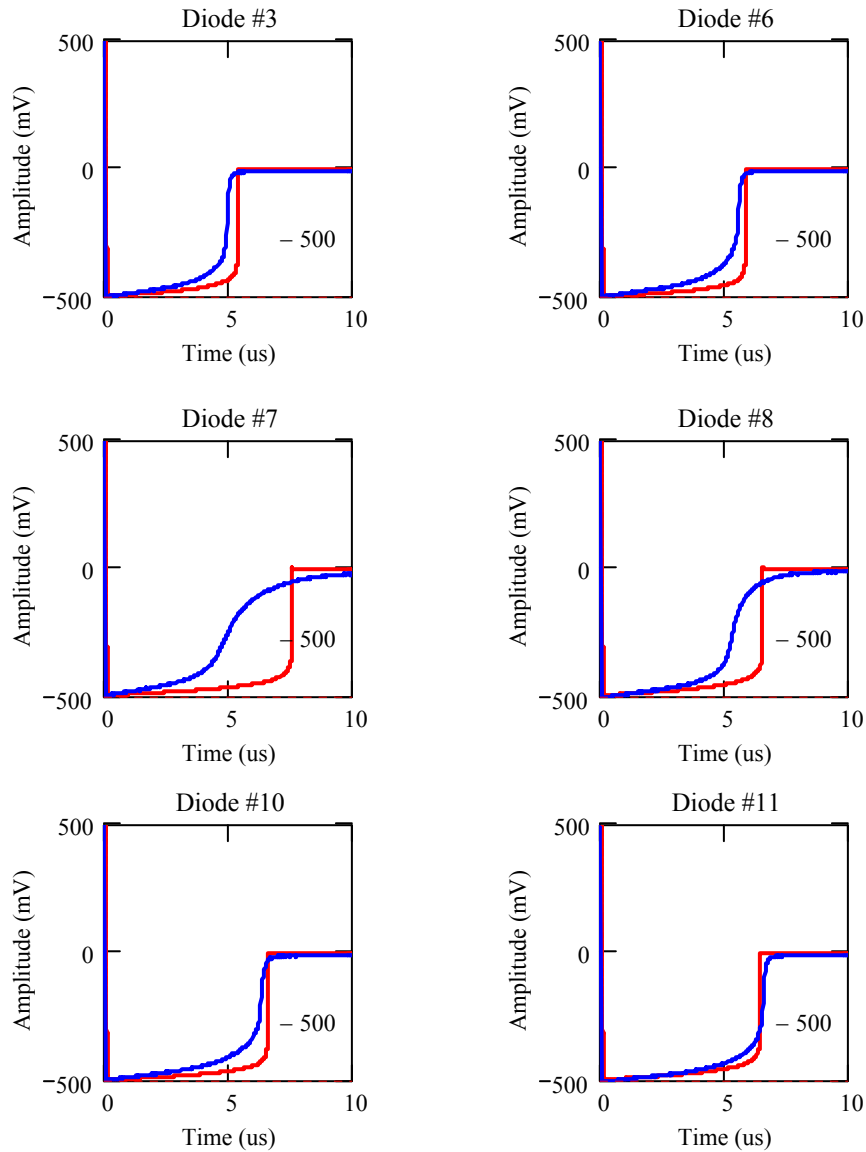


Figure 13 Reverse Recovery Waveforms.

Simulation results are in red and have steep rising edges at the end of the pulse. The measured results are in blue and do not have as sharp a rising edge as the simulation results. The simulation results show sharp recoveries for each diode even though the recovery times are different. The shape of the measured results differed for each diode. The measured result for diode 7 was very different from the simulated result. The SPICE model does not have a mechanism to account for the additional feature observed in the measured result.

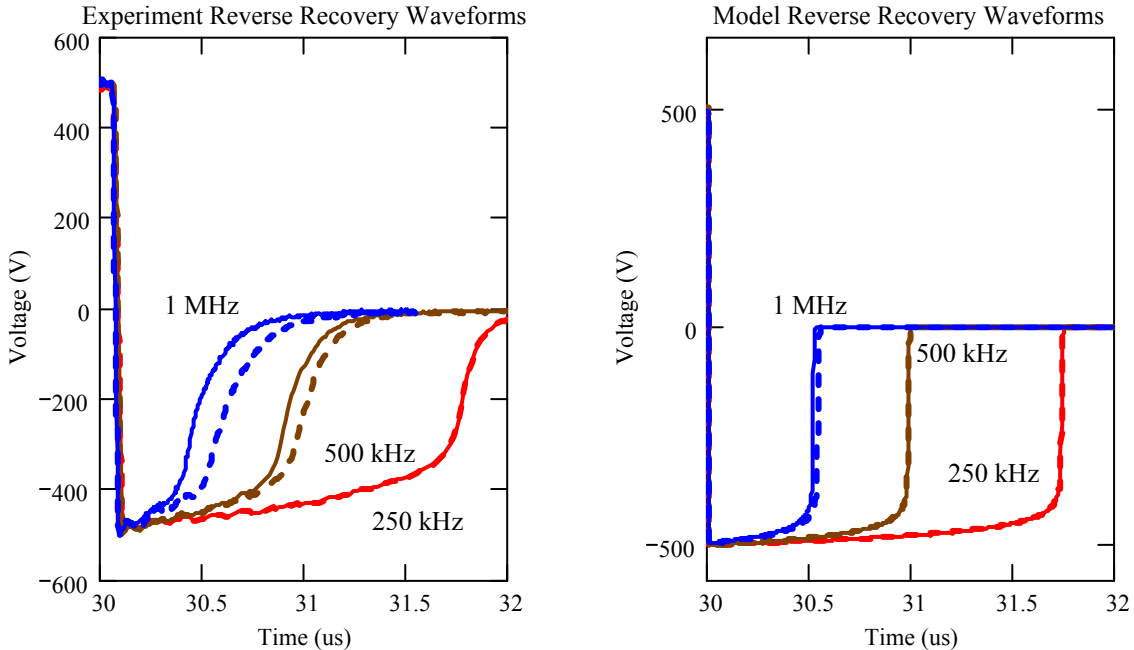


Figure 14 Experiment and simulation results of one versus eight pulses. The solid lines show the recovery response of a single pulse and the dotted lines show the response of the last pulse in a pulse train. The greater drive frequency shows a larger difference between experimental results and measured results.

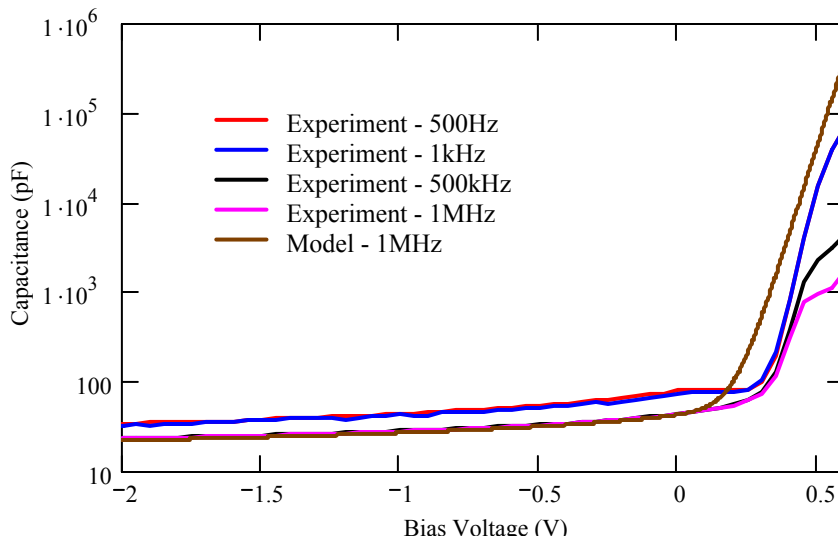


Figure 15 Diode 11 Capacitance

The simulated results of capacitance versus bias voltage do not change with drive frequency. However, the measured results do show that there is a difference in capacitance versus bias for different drive frequencies. This difference in response is a result of the reverse recovery time of the diode and the inability of the model to follow measured results even at moderate frequencies.

Despite the apparent simplicity of the diode resonator circuit (shown in Figure 16), the response of the circuit does behave chaotically at some drive amplitudes and frequencies. The diode resonator circuit consists of a source with a $50\ \Omega$ internal impedance, a $95.6\ \mu\text{H}$ inductor, a diode, and a $20.6\ \Omega$ resistor. The external resistor limits current and functions as a CVR. The results in the report are exclusively from testing with the circuit shown in Figure 16. For each waveform collected, source parameters amplitude and frequency are fixed. Some waveforms across the CVR did not vary from cycle-to-cycle. However, other waveforms had structure that repeated every second, third, fourth, or n^{th} drive cycle.

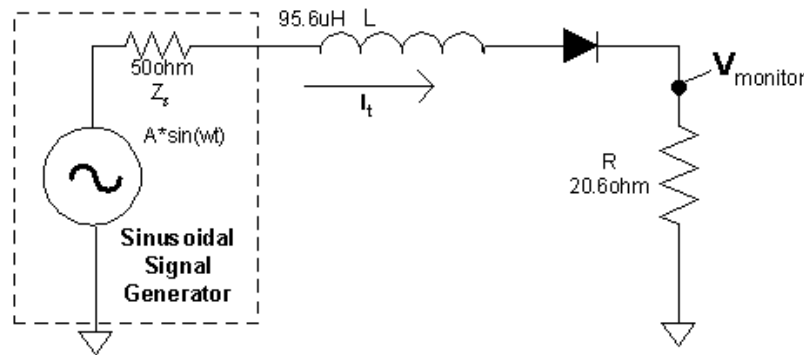


Figure 16 Diode Resonator Circuit commonly referred to as the Linsay Circuit

We conducted part of this study at fixed frequency of 1.22MHz . We obtained data for the bifurcation plots by holding the frequency constant and acquiring a time domain waveform at each drive voltage between 0V and 15V . We determined the maxima for each waveform. We plot all the maxima found for the waveform against the drive voltage. Plotting all the maxima of each waveform makes the bifurcation diagram. Therefore, the bifurcation diagram shows all the maxima values for all the waveforms. Figure 17 and 18 show the bifurcation diagrams for the six diodes tested. Each diode produced different bifurcation plots; however, all the curves have similar characteristics. Each plot shows a single amplitude response below about 1.5V . Just below 1V each diode shows a kink in the curve. The kink occurs where diode starts to conduct. Initial bifurcate for each diode occurs at about 1.5V . Four of the diodes show additional bifurcation at 2V . Diode 8 transitions in and out of chaos in this region. All the diodes then are in a period two state until about 4V where each diode transitions into a period four state. The behavior of each diode is different above this voltage, but the majority transition in and out of chaotic and periodic states. When the drive voltage exceeds 10V all the diodes show chaotic behavior. The diodes remain in a chaotic state up to the maximum drive voltage of 15V .

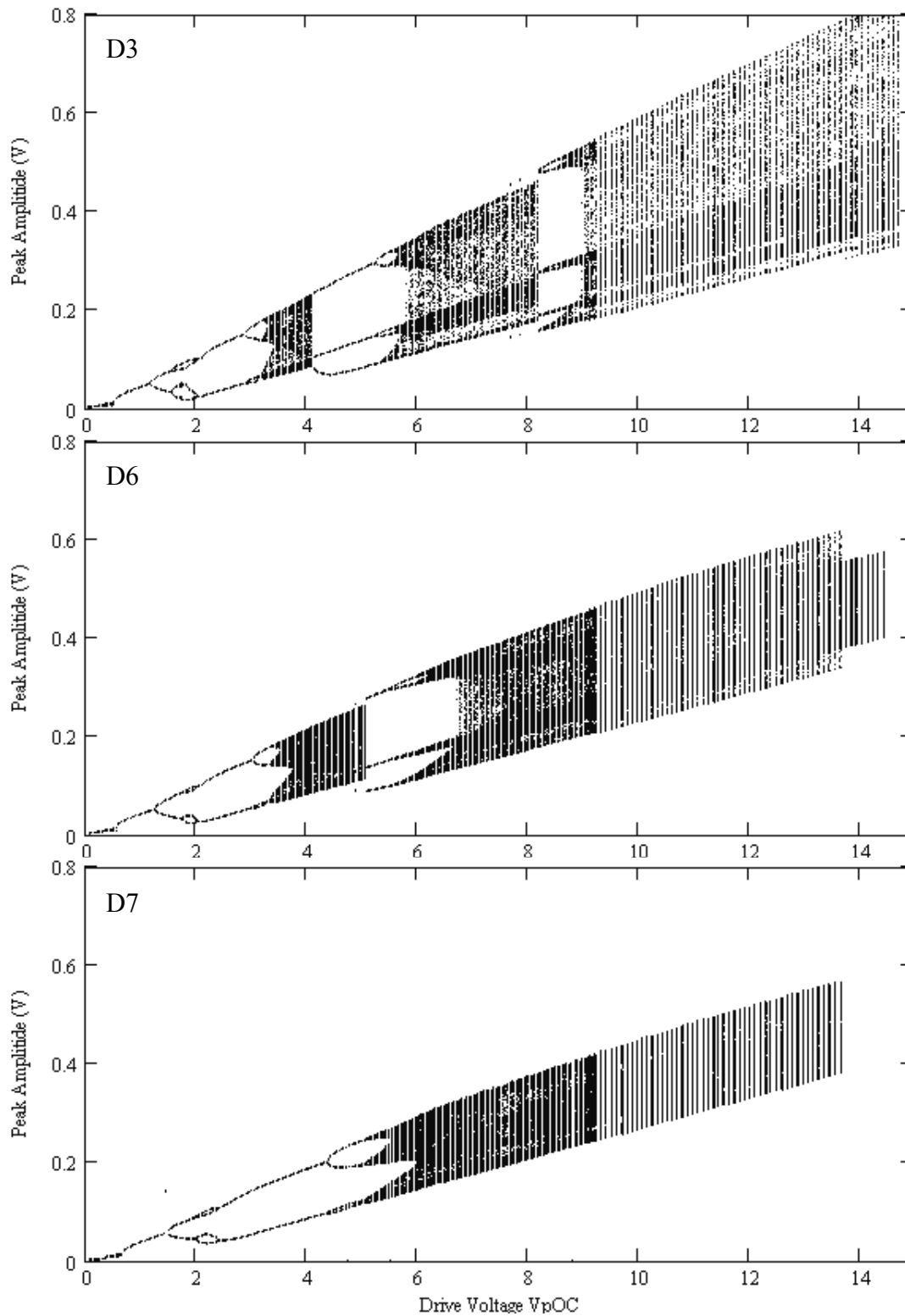


Figure 17 Bifurcation Plot

These plots show the sampled voltage response versus injected voltage of diodes D3, D6, and D7.

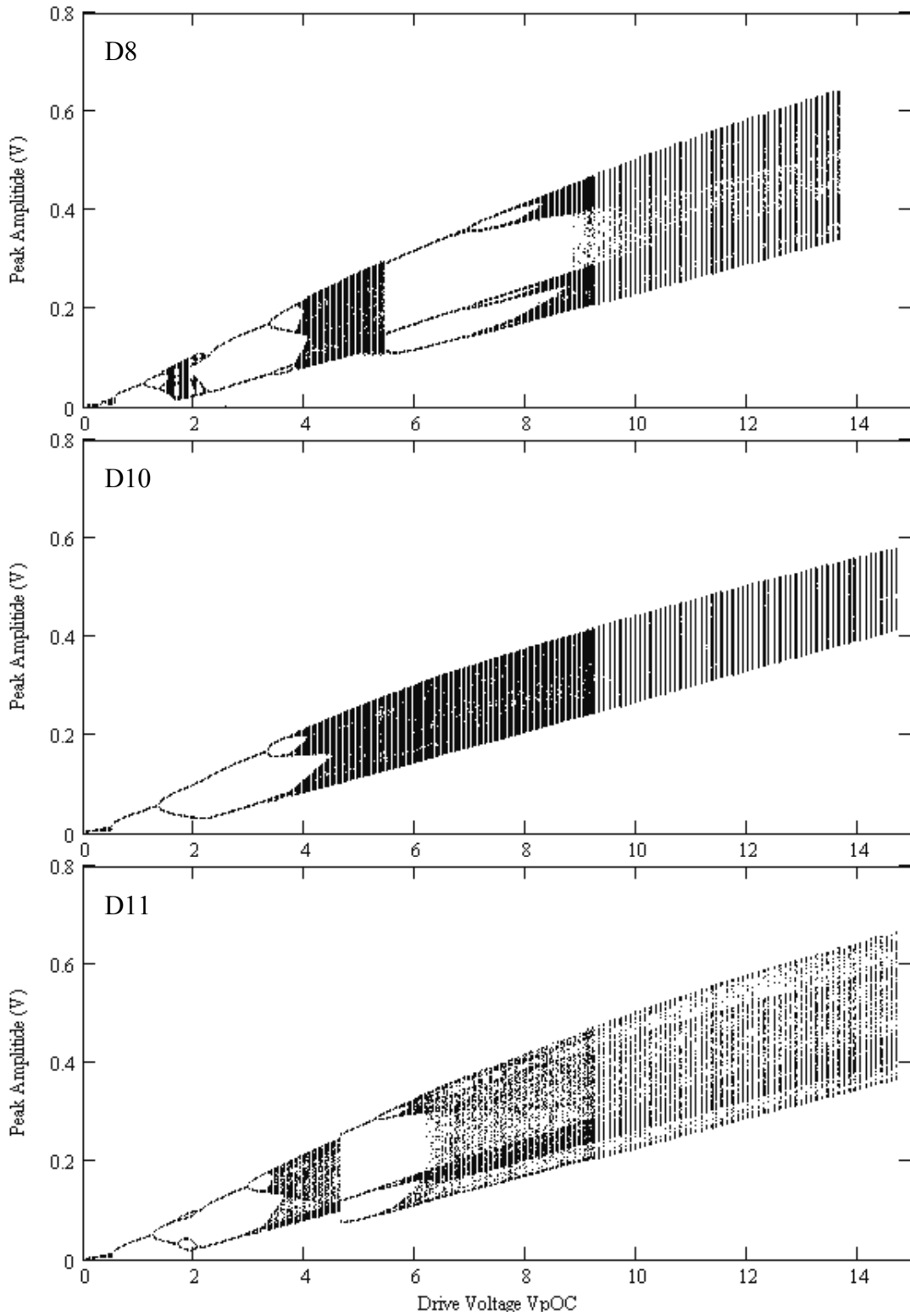


Figure 18 Bifurcation Plot.

These plots show the sampled voltage response versus injected voltage of diodes D8, D10, and D11.

We conducted another series of tests holding the drive voltage constant at 9V. We collected data at frequencies between 10kHz to 5MHz in 10 kHz increments. Figure 21 and Figure 22 show the bifurcation plots. Data from all the diodes showed regions of a single, doubling, and tripling periods. In addition, each diode showed regions of chaos. At low drive frequencies, all six diodes showed a single amplitude response. Between 250 kHz and 500 kHz, Diode 3, 6, and 11 behaved chaotically while Diodes 7, 8, and 10 show a single amplitude response. At about 1 MHz all of the diodes show similar responses. Each diode showed a different response above 1 MHz.

Diode 8 was the only diode that showed chaotic behavior at the upper frequency limit. Diode 7 showed period four response and the remaining four diodes exhibited period two response. Diodes 3, 6, 10 and 11 show amplitude excursions between 2 and 3 MHz. Figure 23 shows the details of these regions. In these regions, the response is periodic surrounded by significant regions of chaotic response. This complex behavior illustrates the frequency sensitivity of the circuits.

The SPICE models produced bifurcation response significantly different than the experiment. The model responses of Diode 3 and Diode 11 are similar to each other, but differ significantly from their experimental results. The two bifurcation diagrams are shown in Figure 19 and 20. The simulations show very similar responses from Diode 3 and Diode 11 contrary to the experimental results. Simulations conducted using frequency as the variable again produced results dissimilar to experimental results. Between 10kHz and 1.5MHz, the frequency bifurcation diagrams of the experiment and the simulations are similar, but the behavior over the entire spectrum is different. Simulations yielded higher average voltages and greater voltage deviations than the experiment. At 10 kHz the experimental results is 0.96V while the simulation result is 1.12V. The maximum experimental amplitude deviation is 0.20V while in the simulation, deviation was 0.50V. These results suggest that the SPICE model for this nonlinear circuit is not a good representation.

Sandia National Laboratories department 01734 (Microsystems Science, Technology & Components) measured the parameters of each diode. 01734 personnel (Jimmie T. Martinez) measured diode transit time as described earlier in this report. 01734 personnel simulated the test circuit using a SPICE simulator. 01734 personnel changed the modeled transit time until the model response matched the measured response. 01734 personnel report the transit time that

produced the best agreement between measurement and simulation. Since the test to measure transit time is performed with a wide pulse, the transit time is valid for low-frequency applications. However, at higher frequencies simulation and measurement results diverge. The theory section of this report provides a more detail explanation for these results. The bifurcation plots we made from scaled simulations agree better with the measurements than the un-scaled simulations agreement with measurements. The bifurcation responses of Diode 8 and 11 are similar.

Figures 21 and 22 show bifurcation diagrams with drive frequency as the parameter. We measured these bifurcation diagrams using a fixed peak drive voltage of 4.55 V. These results show that the chaotic behavior of the circuit also depends on drive frequency. Figure 23 shows a blow up of the results shown in Figures 21 and 22. These blow-ups show the detail of the circuit transitions between periodic behavior and chaotic behavior with extremely small drive frequency changes.

Our first goal was to determine the mechanism of chaotic behavior. We believe we have a good working theory. Our models produced simulation results that were consistent with our experimental results. Further, we wanted to determine whether understanding chaotic behavior could lead to a better understand of disrupting electronic circuits at lower RF energy levels. This goal was more elusive. Although we did not find lower thresholds of circuit disruption, it is clear from our results that the possibility of lower threshold exists. The possibility of lower thresholds is evident in the range of responses these circuits exhibited when parameters of the stimulus is changed.

We confirmed results obtained by other researchers. In addition, we developed a theory and model that produced much closer agreement between simulation results and measured results. Although other researchers showed that the Linsay circuit exhibits chaotic behavior, simulations and experimentation results do not agree (amplitude, spectral content, and Lyapunov number, etc.). By implementing corrections to some model parameters, we obtained better agreement between simulated and measured than without the corrections.

Although we have a working model of the chaotic behavior of the Linsay circuit much more needs to be done. The current circuit based model is not robust and we would like to produce a physics based model. The current model contains parameters that must be altered for

variations in drive frequency and amplitude. A physics based model would address fundamental properties of the pn junction.

With the improvement in computing power and the need to model circuit behavior with greater precision, the nonlinear effects of circuit has become very important. In addition, every integrated circuit has as part of its design a protective circuit. These projective circuits use some variation of semiconductor junctions that can interact with parasitic components, present in every real system. Hence, the protective circuit can behave as a Linsay circuit.

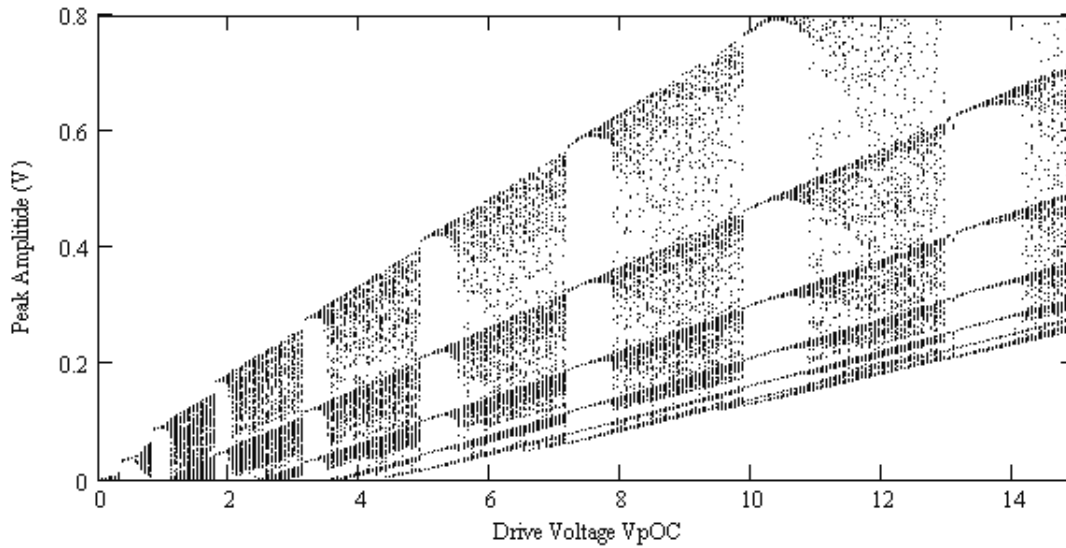


Figure 19 Simulation Bifurcation Plot (Un-scaled t_{rr})

This figure shows un-scaled simulation results. These results differ significantly from measured results shown in Figures 17 and 18.

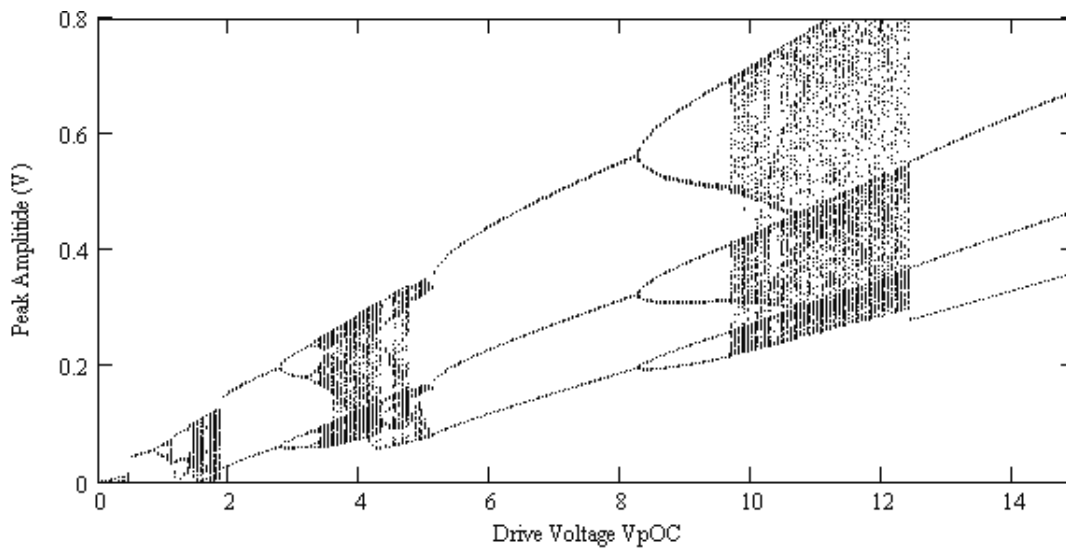


Figure 20 Simulation Bifurcation Plot (Scaled t_{rr})

The figure shows the scaled simulation result that is similar to measured results found in Figures 17 and 18.

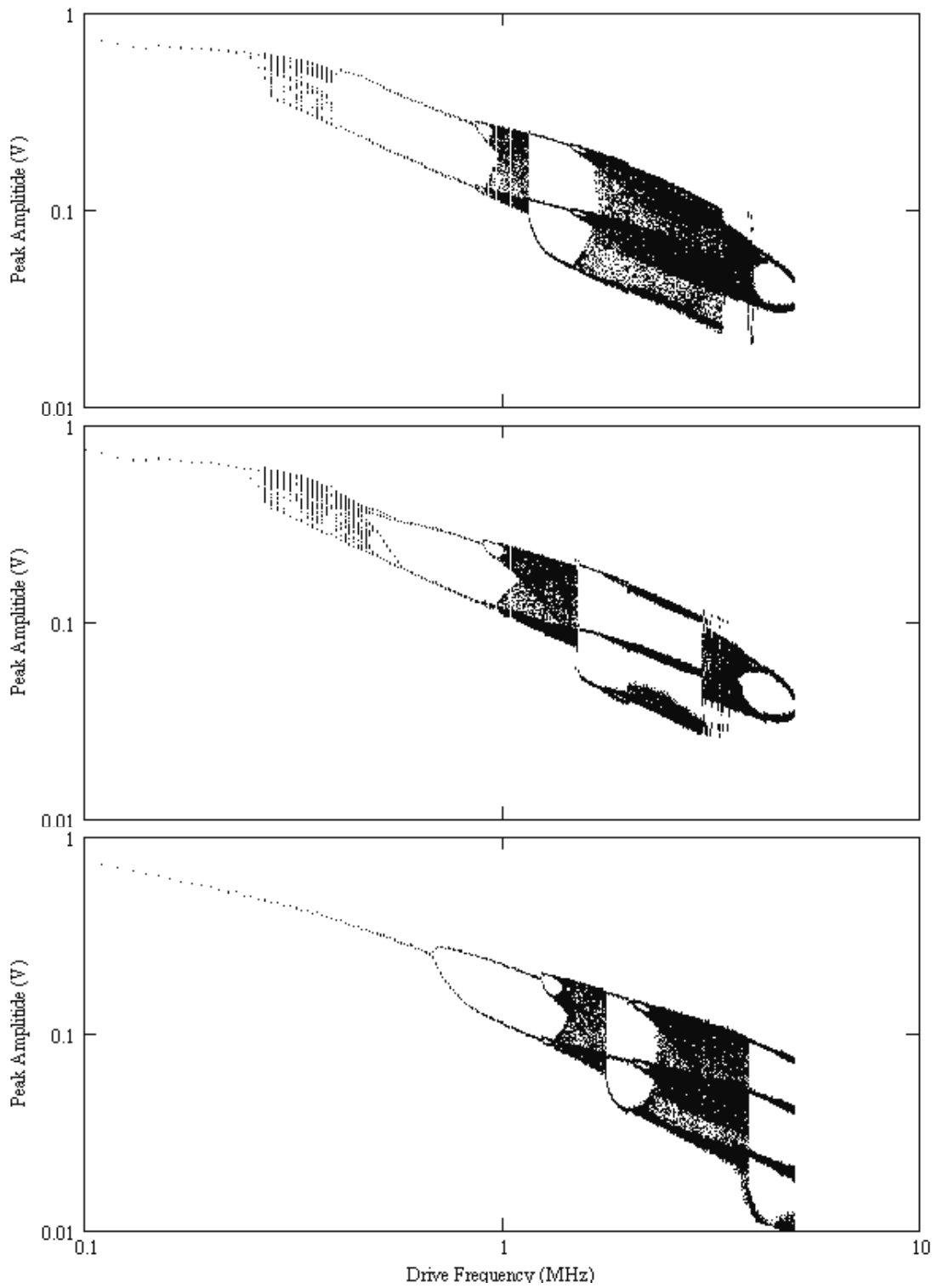


Figure 21 Diodes 3, 6, and 7 Frequency Bifurcation Plots

In these plots, the drive voltage is held constant and the drive frequency is varied. As with the voltage bifurcations plots, the response transitions between periodic and chaotic behavior.

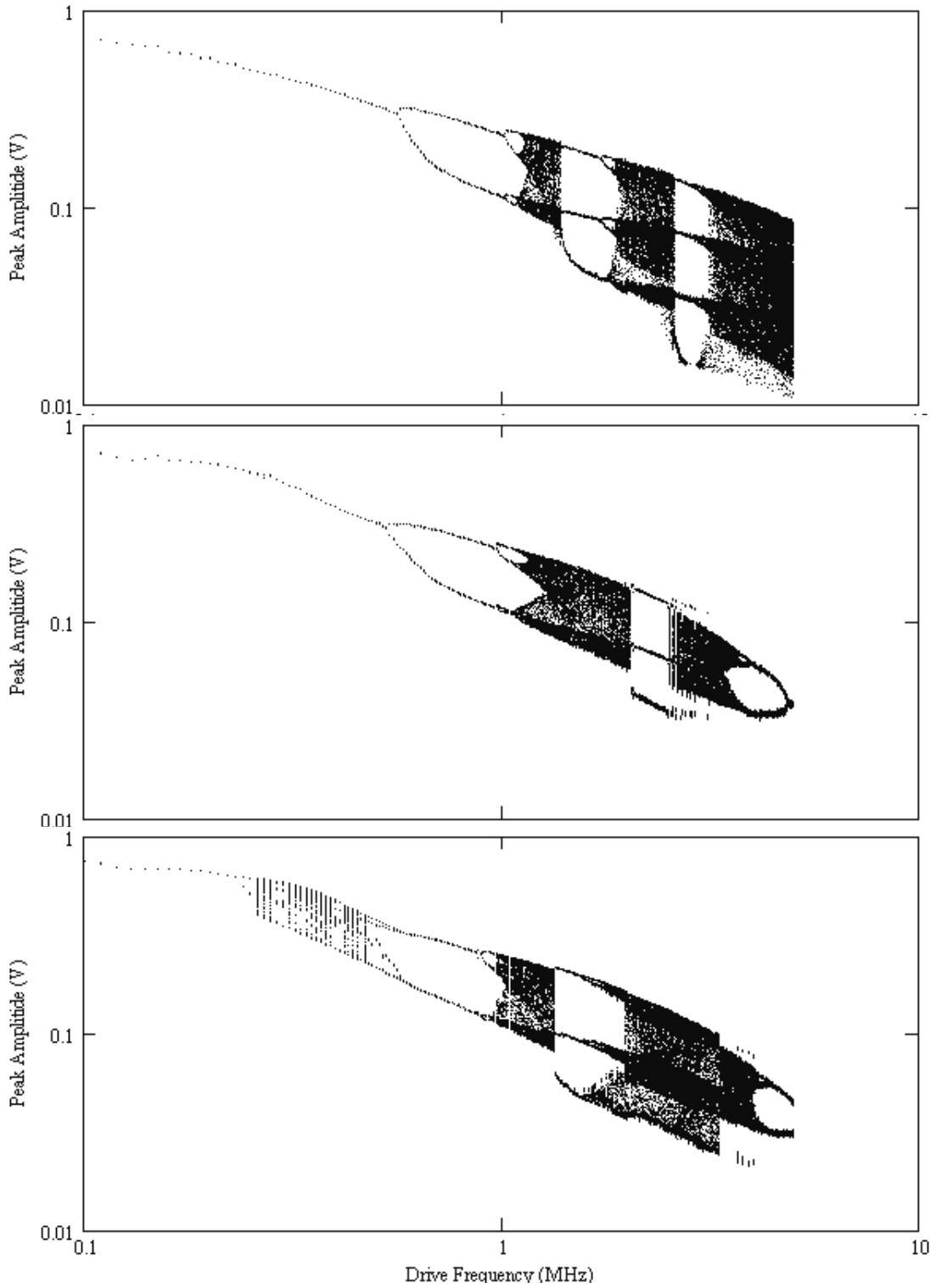


Figure 22 Diodes 8, 10, and 11 Frequency Bifurcation Plots
 In these plots, the drive voltage is held constant and the drive frequency is varied. As with the voltage bifurcations plots, the response transitions between period and chaotic behavior.

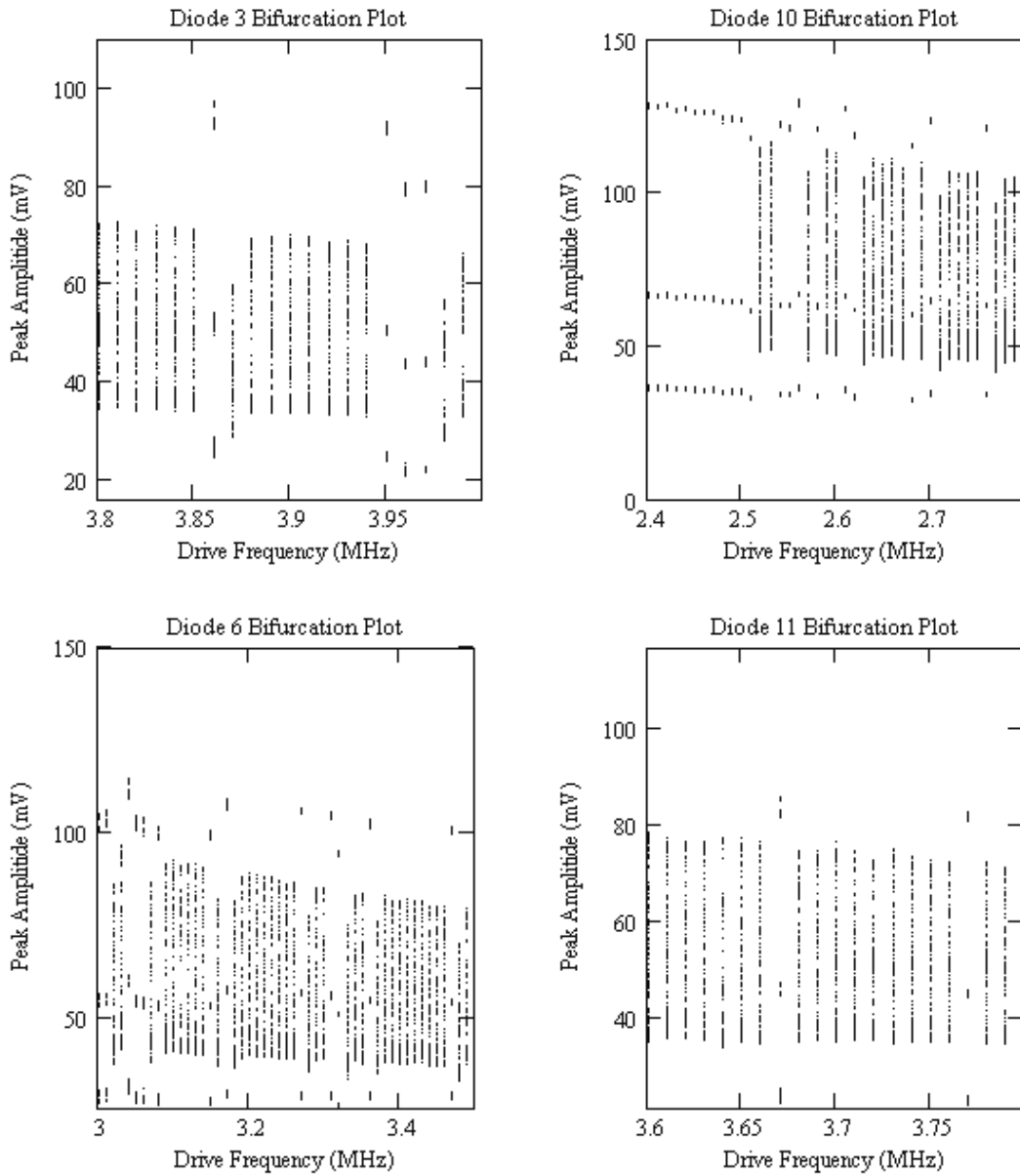


Figure 23 Frequency Bifurcation Details for Diodes 3, 6, 10, and 11. This figure shows a blowup of Figures 21 and 22. On this frequency scale, one can see how readily the circuit response can change from periodic to chaotic.

Phase-Locked Loop

Phase-Locked Loop Theory

We also studied the nonlinear behavior of a phased-locked-loop. Phased-locked loops are fundamental building block to many major systems (aileron, seeker heads, etc). In this section, we show that an injected RF signal can drive a phased-locked-loop into chaos. While the RF is injected into the circuit, the frequency of the phased-locked-loop leaves its normal range of operation. In addition to the time the RF drives the phased-locked-loop out of its normal range of operation, additional time is needed for the phased-locked-loop to return to its normal operation. The RF signal only needs to disturbance the phased-locked-loop long enough to cause the phased-locked-loop to leave its normal range of operation, and the disturbance only needs to occur often enough to keep the phased-locked-loop from returning to its normal operating range. Hence, a pulsed RF signal with sufficient pulse repetition frequency can cause a phased-locked-loop to go into a chaotic state and stay in a chaotic state until the RF signal stops.

Phase-lock-looped (PLL) circuits are a basic part of many control systems. In addition, a PLL can control the frequency of a transmitter and receiver of a radio. The block diagram of a PLL, shown in Figure 24, consists of a phase detector, loop filter, loop amplifier, and a voltage-controlled-oscillator (VCO).

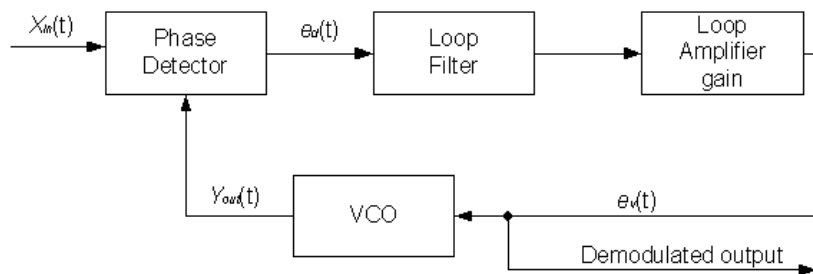


Figure 24 Diagram of a Phase-Locked Loop

Refer to Figure 24 for the following discussion. A PLL drives the phase difference between the input carrier, $X_{in}(t)$, and the output of the VCO, $Y_{out}(t)$, to zero. A PLL, as the

name implies, locks the difference between two signals. In order to understand how a PLL works consider the following. The following represents the input signal:

$$X_{in}(t) = A_{in} \sin(\omega_c t + \phi(t)).$$

The VCO output, or reference signal is represented as:

$$e_o(t) = -A_{VCO} \sin(\omega_c t + \theta(t)).$$

The frequency deviation of the VCO is proportional to its input, $e_v(t)$;

$$\frac{d\theta(t)}{dt} = K_v e_v(t),$$

where K_v is the VCO gain.

$$e_d(\psi) = K_d \sin(\psi),$$

where $\psi = \phi(t) - \theta(t)$ is the phase error and K_d is the proportionality constant.

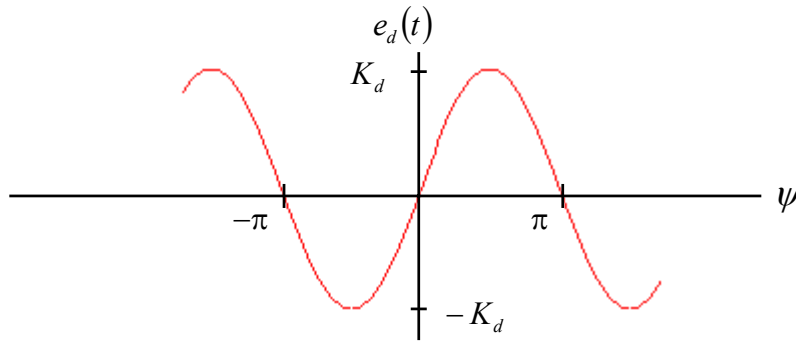


Figure 25 Phase-Plane Plot

Assume that the PLL operates in the linear range of $e_d(t)$ $\left(-\frac{\pi}{2}, \frac{\pi}{2}\right)$. Then the following is derived using control theory.

$$E_d(s) = K_d(\Phi(s) - \theta(s)) = K_d \psi(s)$$

$$E_v(s) = F(s) E_s(s)$$

$$\theta(s) = \frac{K_v E_v}{s}$$

With some mathematic manipulation, we derive the following. The closed-loop transfer function is:

$$H(s) = \frac{\theta(s)}{\Phi(s)} = \frac{K_v K_d F(s)}{s + K_v K_d F(s)}$$

The phase error transfer function is:

$$H_e(s) = 1 - H(s) = \frac{s}{s + K_v K_d F(s)}$$

The VCO control-voltage/input-phase transfer function is:

$$H_v(s) = \frac{s K_d F(s)}{s + K_v K_d F(s)}$$

Phase-Locked Loop Application

Phase lock loops are in a great number of electrical devices. A single IC and a few passive components comprise a large percentage of these PLLs. For example, PLLs are in phase or frequency demodulators, as well as, frequency synthesizers. Examples of two demodulator PLL integrated circuits are the LM565C and the 74HC7046A. Shown in Figure 26 is a schematic diagram of a simple 74HC7046A PLL circuit.

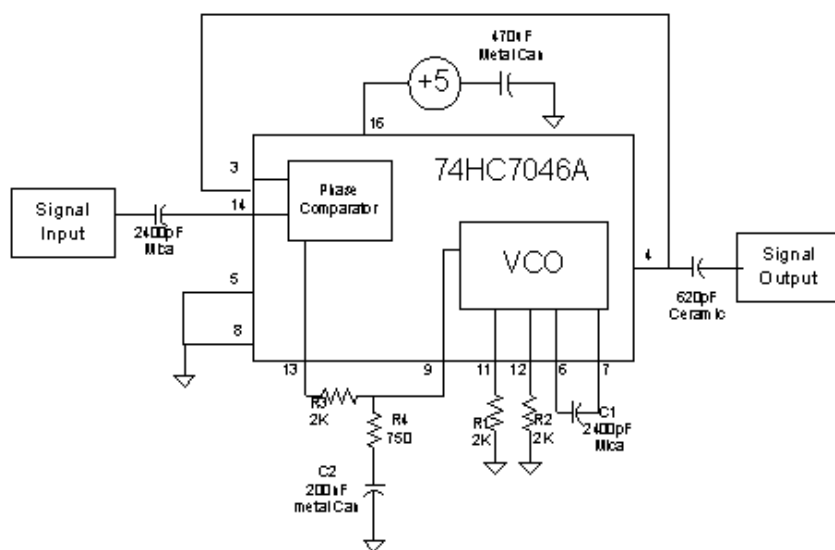


Figure 26 74HC7046A PLL Circuit

The above theory applies when the PLL is in the linear range of operation. Conditions exist that can cause the PLL to leave the linear range and enter the nonlinear region shown in Figure 25. In Tetsuro Endo's paper, *Chaos From Phase-Locked Loops*¹⁰, Endo states that a PLL can enter a chaotic state when driven outside its normal operating range. Experimental results from this paper show that even a small phase deviation of the input signal was enough to cause the PLL to become chaotic when the PLL was close to its critical detuning (pull-in range).

In preliminary testing of the LM565C and 74HC7046A PLL, results support the Endo's theory. When the input carrier frequency was close to the extremes of the tuning range of the PLL, any small phase modulation caused the PLL to lose lock. Out of lock, the noise floor of the PLL's frequency spectrum increases to fill the surrounding spectra suggesting that the PLL was exhibiting chaotic behavior.

During operation, PLL spectral output is essentially a single frequency. The error voltage feed into the local VCO maintains a constant phase. Outside the normal operation range, the error voltage attempts to correct the phase of the VCO, but the VCO is unable to properly respond since it is now attempting to operate outside its normal range.

The operating frequency range of the 74HC7046A PLL IC is 40MHz. The PLL shown in Figure 26 above has a free running frequency of 8.3 MHz and a pull in range of 500 kHz. Figure 27 shows the test results of a 74HC7046A PLL driven with three drive frequencies; one just

below the normal range of operation (8.3 MHz), one in the normal range of operation and one above the normal range of operation. When operated in the normal range of operation, the PLL output was a narrow. When outside its normal range of operation, the spectrum of the PLL spread out.

FRS radios, GPS systems, & cellular telephones use frequency synthesizers because stable frequency is crucial. A PLL has a designed frequency range of operation. Once the PLL is outside its operation range, the PLL either ceases operation or behaves chaotically. We conducted testing on a Motorola MC145220 evaluation board and a Radio Shack FRS radio. The PLL in both systems responded as shown in Figure 27. What Figure 27 shows is that the operating frequency shifted and broadened. A radio will not function with this interference. Hence, both radios were disabled.

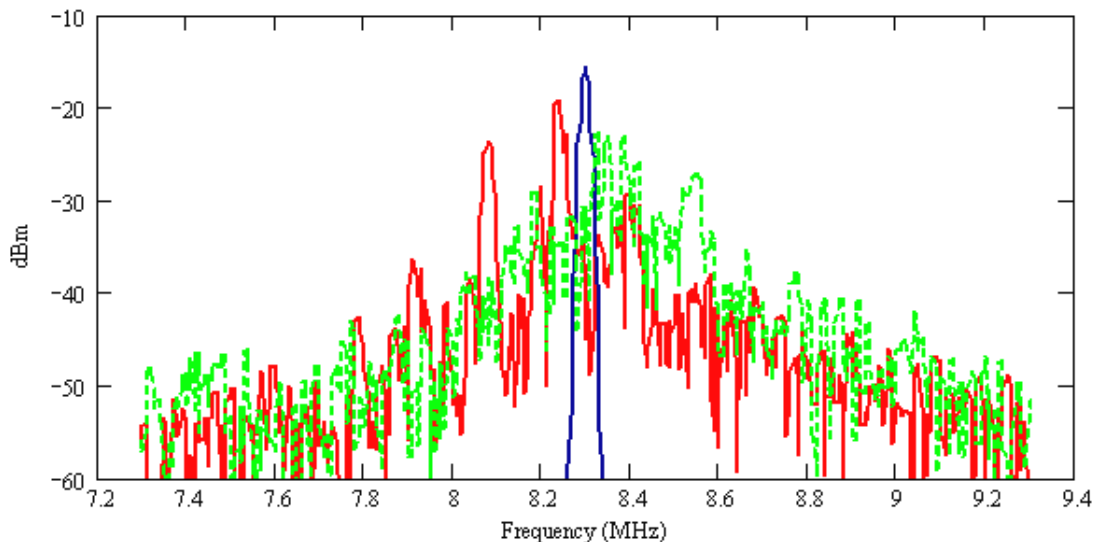


Figure 27 74HC7046A Swept Frequency Test.

The blue trace shows the narrow frequency response of the PLL during normal operation. The red trace (below the normal PLL frequency) and green trace (above the normal PLL frequency) show the response of the PLL while subjected to RF.

The Motorola MC145220 evaluation board has two channels. Each channel is capable of generating RF frequencies between 600 MHz to 950 MHz. The MC145220 PLL chip has a operating range of 40 MHz to 1100 MHz. The two channel error voltages from the PLL chip control the two frequency oscillators located underneath the evaluation board. The VCOs limit the frequency ranges of the evaluation board. The digitally programming of the MC145220 determines the output frequency of the two synthesizer channels.

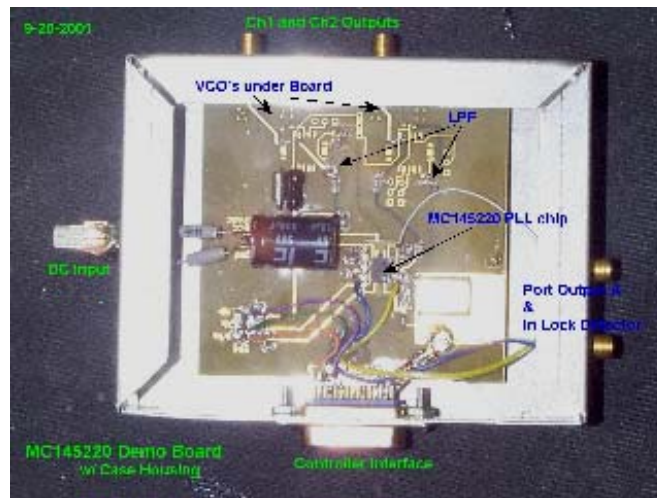


Figure 28 MC145220 Motorola Evaluation Board used to measure PLL response

The MC145220 has two on-chip dual-modulus prescalers, independently programmed to divide by 32/33 or 64/65. Logic sections of the MC145220 divide channel 1, channel 2, and the reference frequency signals to a common compare frequency through divide-by-N flip-flops. The phase comparator of each channel compares the phase difference between the two divided down signals, channel 1 and reference or channel 2 and reference, and outputs an error voltage related to their phase difference. The error voltage then adjusts the external VCO for that particular channel. We program the synthesizer, via a synchronous serial connection, to control the divide number used by the MC145220.

We built a controller to program the IC via a serial bus. The controller programs the FIFO configuration of the five different registers of the IC; the reference register, access registers (channel 1 & 2), and the configuration registers (channel 1 & 2). The controller also provided the lock indicator.

We magnetically coupled RF energy to test PLL using a test probe made from a two-turn loop of magnetic wire, 3/16" in diameter. The signal generator that drove the probe operated between 100k-2112 MHz. The maximum signal generator power was 20 dBm. In similar previous tests we found that when focusing the coil at particular regions of the PLL, a 1 kHz-2 μ s pulsed, 800 MHz signal radiated signal disturbed circuit operation. The spectra output of both the Radio Shack and Motorola test circuits were similar. The Motorola was more sensitive in the physical area of the low pass filter. When stimulated the spectrum of the PLL shift downward.

MC145220 Demo Board

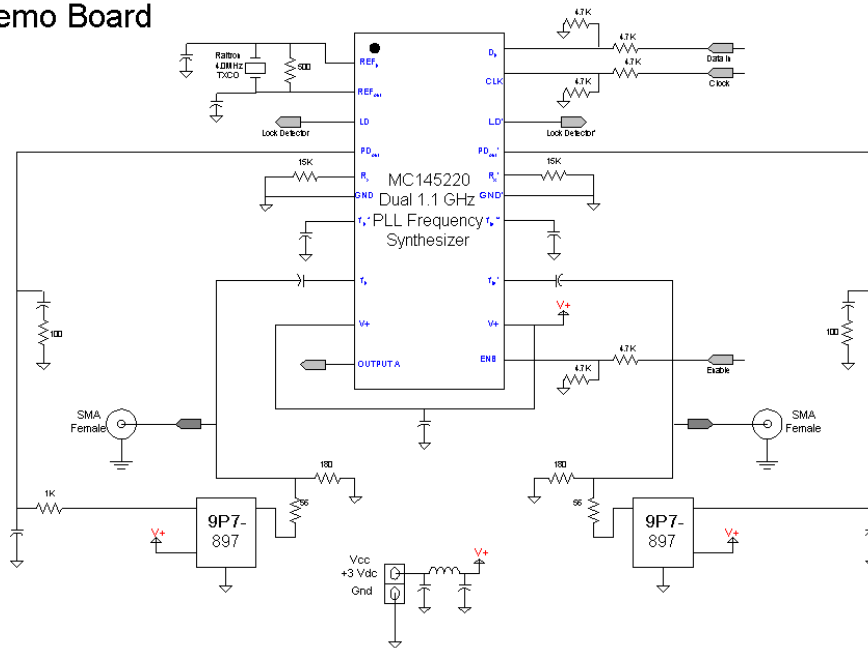


Figure 29 MC135220 Motorola Evaluation Board Schematic
Used to measure PLL response

The Radio Shack FRS radio, catalog 21-1810, contained two primary PC boards. The bigger of the two boards contained; the digital signal processor controller, the audio, and dual tone multiple frequency filtering subsystems. The smaller board contained the PLL, RF heterodyning, and RF amplification. For these tests, we removed the small RF board from FRS radio and connected to an external digital controller developed for the MC145220. Separating the RF board from the DSP controller board of the FRS radio allows us to subject the PLL to RF tests with minimum effect on the digital control circuit.

The PLL of the RF board uses a Toshiba TB31202FN PLL IC. This IC has two independent PLL channels to control the receiver and transmitter sub-circuits. The VCO of the transmitting section is a Colpitts oscillator. The capacitances, of two tuner diodes, determine the frequency. The voltages, across the diodes, determine the capacitances of the diodes; Hence, the frequencies are controlled by applied voltages. The diode capacitance is inversely proportional to the voltage applied, and to the frequency. An input control voltage of 24 mV to 3.0 V produces a range of 453.16 MHz to 562.0 MHz. After amplification, the oscillator output drives the Toshiba TB31202FN PLL IC.

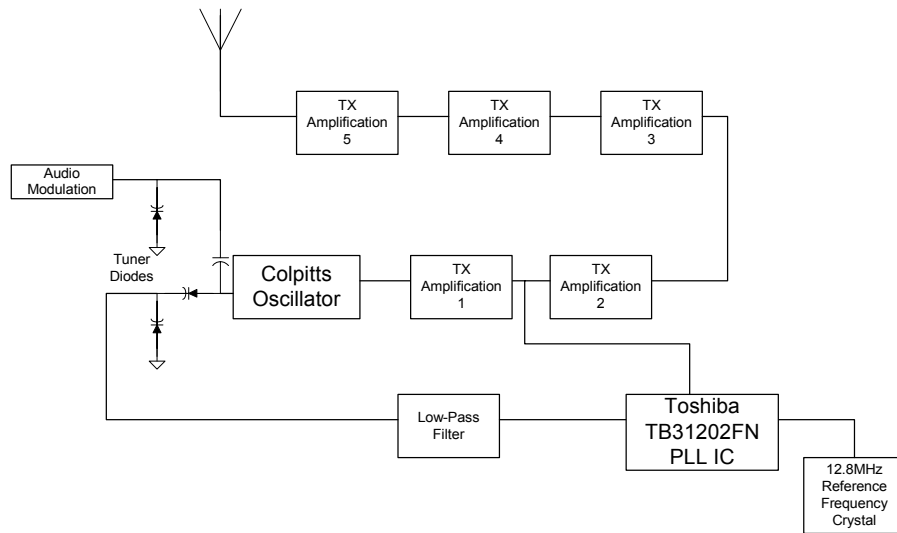


Figure 30 Block Diagram of the Radio Shack FRS Radio RF Section Used to measure PLL response

The Toshiba TB31202FN has two independent channels each with its own prescaler and PLL. Designed to work between 200 MHz and 500 MHz, the TB31202FN uses a charge pump to bias the two tuner diodes of the Colpitts oscillator. The IC uses a 12.8 MHz reference signal from a crystal oscillator. 6.25 kHz is produced by dividing the reference signal by 2048. When the FRS radio is set on channel 5 (462.6625 MHz), the VCO output is 6.25 kHz by dividing the channel frequency by 74026 ($32 \times 2313 + 10$). The phase comparator compares two 6.25 kHz signals and adjusts the potential that controls the RF outputs to synchronize the two signals. The low-pass-filter frequency cutoff is 420Hz. The voltage across the tuner diodes adjusts the capacitance of the VCO, which in turn adjusts the frequency of oscillation.

Using the RF coupler used earlier on the MC145220 evaluation board, we found that a 1 kHz-2 μ s 800 MHz RF pulse directed into the base of the Colpitts transistor caused the spectrum of the radio to shifting down about 300 kHz and broadening to a bandwidth about 70k Hz. The shift and broadening depends on the amount of RF power coupled to the oscillator. At higher RF power, the effect was greater. We recorded several megahertz deflection and several kilohertz a broadening when injecting higher RF powers. Figure 32 illustrates spectral response of the 300 kHz shift and 70 kHz broadening.

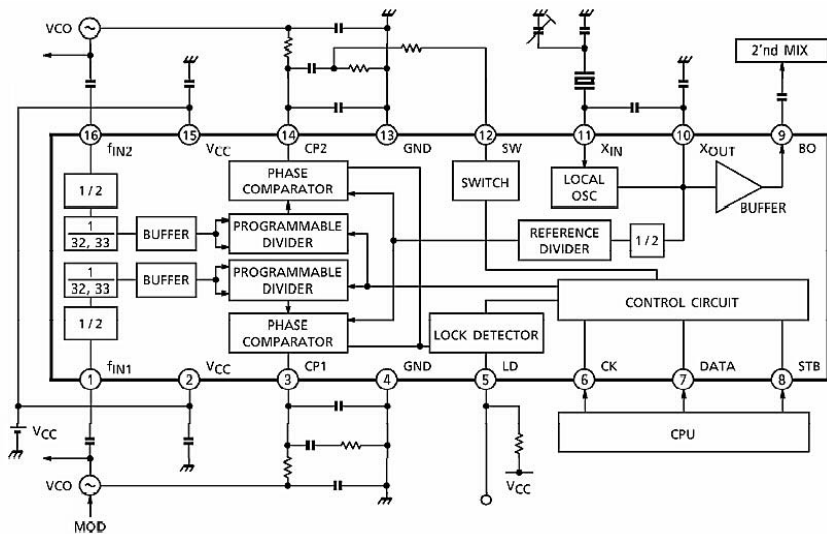


Figure 31 Block Diagram of the Toshiba TB31202FN IC the PLL chip Used in the Radio Shack FRS Radio

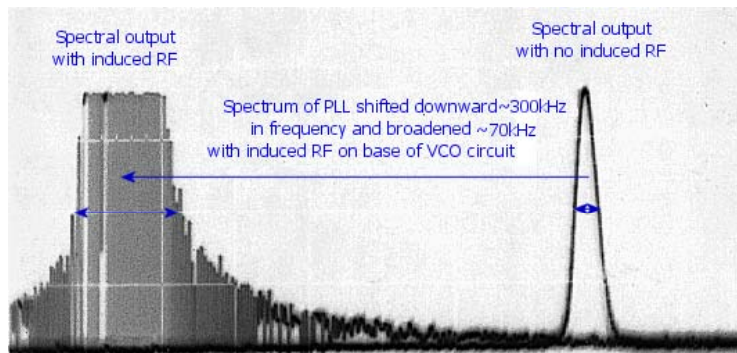


Figure 32 Spectral Shifting and Broadening

Response of the PLL in the Radio Shack FRS radio to injected RF. The spectral response on the right is the normal PLL frequency response. The spectral response on the left is the response when the PLL is subjected to RF.

We used several methods to examine the induced effects on the PLL. First, we observed the error voltage on the output of the low-pass filter; the error voltage controls the VCO. A single $1\mu\text{s}$ wide 800 MHz pulse caused the error voltage to deflect less than 2 mV. When exposed to an RF (800 MHz) $2\mu\text{s}$ pulse at a 1 kHz repetition rate, 7 mV peak-to-peak and DC voltage of -80 mV was superimposed across the tuner diodes. The AC component caused the wideband response, and the DC offset lowered the frequency range of the VCO. A rapidly changing error voltage causes frequency to change rapidly. Higher injection RF energy increased the DC deflection and AC component of the error voltage.

Radio Shack FRS radio 21-1810
RF PCB

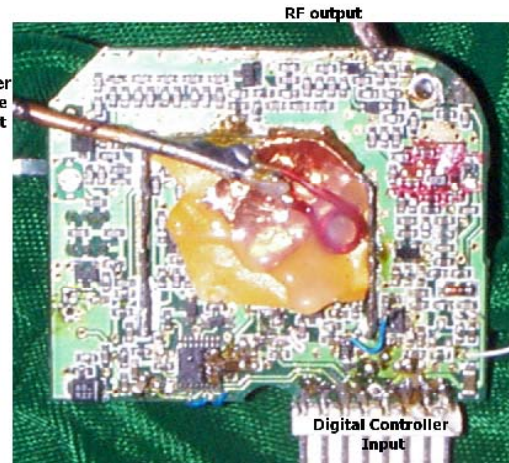
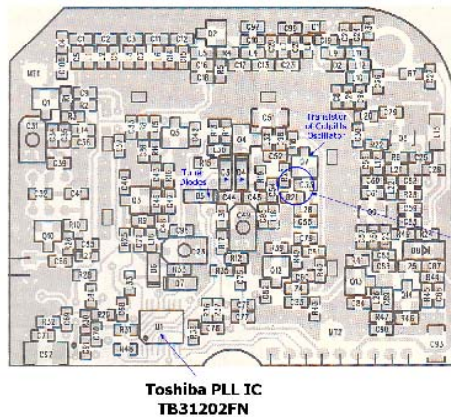


Figure 33 RF PCB Section of Radio Shack FRS Radio

The duty cycle and peak power of the RF pulses determine the average radiated power. Increased average power increased the disturbance of the PLL. With a source power of 2.0 dBm and a single 1 μ s pulse, the error voltage dipped less than 2 mV. The error voltage quickly recovered and returned to its original voltage level. Increased pulse-widths caused greater deflection and at 200 μ s the error voltage dipped more than 50 mV. The PLL recovery time is 11 ms for the 1 μ s pulse and 21 ms for the 200 μ s pulse. A 50 mV error voltage drop causes the VCO output to drop 5 MHz. Increasing power from 2.0 dBm to 4.5 dBm, pulse width of 200 μ s, the error voltage dips more than 64 mV and the recovery time of the circuit is 20 ms

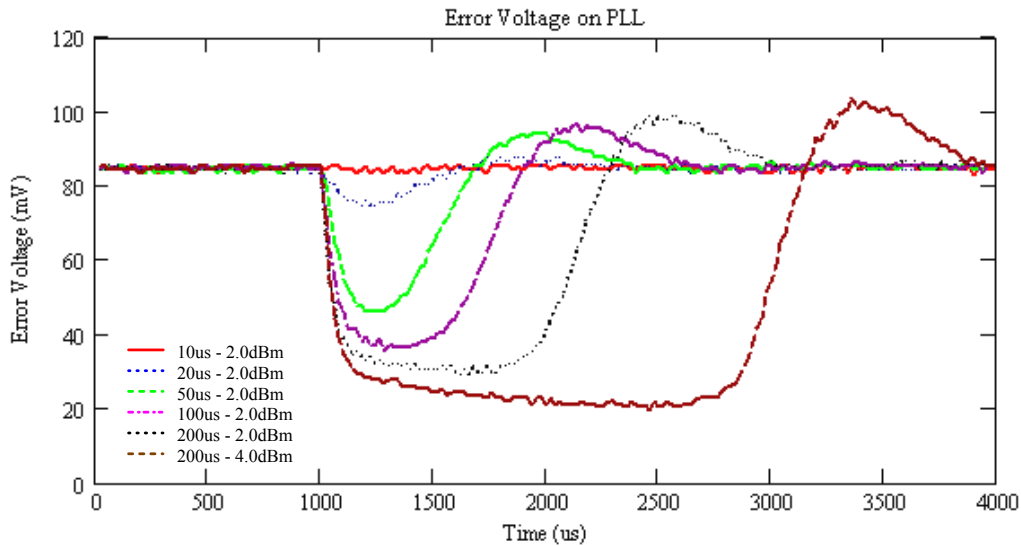


Figure 34 Time Waveforms of the PLL

Plot of Error Voltage versus RF Pulse-Width / Drive Levels. As the drive power and pulsewidth increase the duration that the error voltage deviates from normal increases.

Both a continuous and pulsed RF effect the PLL operating frequency. An error voltage of 0.84V causes the VCO to operate at its normal frequency of 462 MHz. We varied the drive frequency and drive power level between 1.0 MHz to 1.0 GHz and 0 dBm to 20 dBm. The injected signals that caused the error voltage varied between 0V and 3.0V, which is the full range of the power supply. Hence, the PLL power supply limited the error voltage range.

Shown in Figure 35 is PLL error voltage as a function of injected frequency. At frequencies less than 200 MHz, and any power level, the PLL error voltage does not alter from its nominal 0.84V. Above 200 MHz the error voltage begins to droop then rise dramatically about 462 MHz (PLL normal frequency). At higher drive frequencies, the injected signal causes sufficient error voltage deflection to drive the VCO frequency outside the 10 kHz the FRS channel. The error voltage range of 0V to 3.0V corresponds to a frequency range of 453 MHz to 562 MHz. In Figure 35, it appears that a disruption frequency around the channel frequency, or its harmonic at 924 MHz, is most effective at disturbing the error voltage.

In the regions where the PLL error voltage deviated from its normal range, the error voltage; and hence, the PLL was chaotic. Since the error voltage drives the PLL frequency, the output frequency of the PLL was also chaotic.

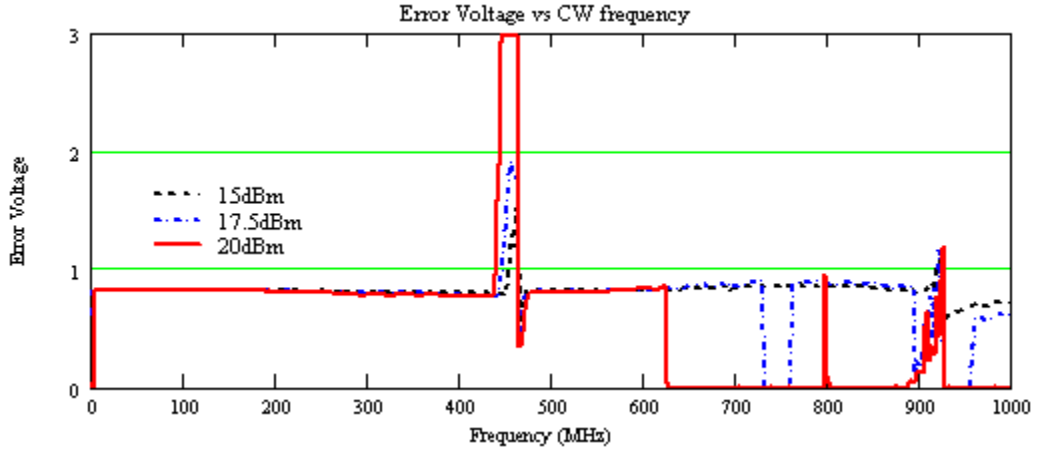


Figure 35 Error Voltage Response with Changing Drive Frequency (CW)

In this figure we see that as the drive frequency increases the error voltage changes. Around the normal operating frequency of 462 MHz, the error voltage deviates significantly from normal and is limited by the voltage of the power supply. In these frequency ranges, the PLL is behaving chaotically. At even higher frequencies, the error voltage drops to zero. The reason for this behavior is that the external RF source is driving the frequency counter on the PLL off of its normal frequency and the PLL circuit is trying to correct for the offset frequency. Since the frequency measured by the frequency counter is not related to the frequency of the PLL, the error circuit continues to drive the error voltage until the voltage cannot change any more.

In addition to the direct injection testing discussed above, we conducted tests on the Radio Shack radio at 95 GHz to investigate high frequency effects on the PLL. The manufacturer is CPI. The model number of the source and power supply was VKB2426L3 and VPW2838 respectively. The radar range equation for the 95 GHz test setup in terms of dB is $P_R = P_{source} + G_{Millitech} + L_{path} + A_R - L_{PScoupling} - L_{TXline} - L_{Aerowave}$, where P_R is the power measured by an Hewlett Packard 436A power meter, P_{source} is source power, $G_{Millitech}$ is Millitech transmitting antenna gain, L_{path} is path loss, $L_{PScoupling}$ is excess sensor coupling loss, L_{TXline} is transmission line loss, and $L_{Aerowave}$ is Aerowave power divider loss. The effective area A_R of the receiver is

$$A_R = G_{receive} + 10 \log \left(\frac{\lambda^2}{4\pi} \right),$$

where $G_{receive}$ is the receive antenna gain. $P_{source} = 46.8 \text{ dBm}$, $L_{TXline} = 0.4 \text{ dB}$, $G_{milltech} = 24.0 \text{ dB}$, $L_{path} = 10 \log\left(\frac{1}{4\pi d^2}\right)$, $G_{receive} = 6.0 \text{ dB}$, $L_{Aerowave} = 34.0 \text{ dB}$, $L_{PScoupling} = 1.4 \text{ dB}$.

The distance between the transmitter and the receiver antenna is 'd' and wavelength $\lambda = 0.32 \text{ cm}$. The power density at the receiver antenna using linear expressions is:

$$P_{density} = \frac{P_{source} G_{milltech} L_{TXLine}}{4\pi R^2}$$

The 95 GHz test setup focused energy directly onto the VCO section of the PLL board. To pulse modulate the RF, we used a chopper disc with 50% opening. When the chopper rotates, it creates a 50% duty cycle RF pulse train. The maximum chopping rate is 750 Hz.

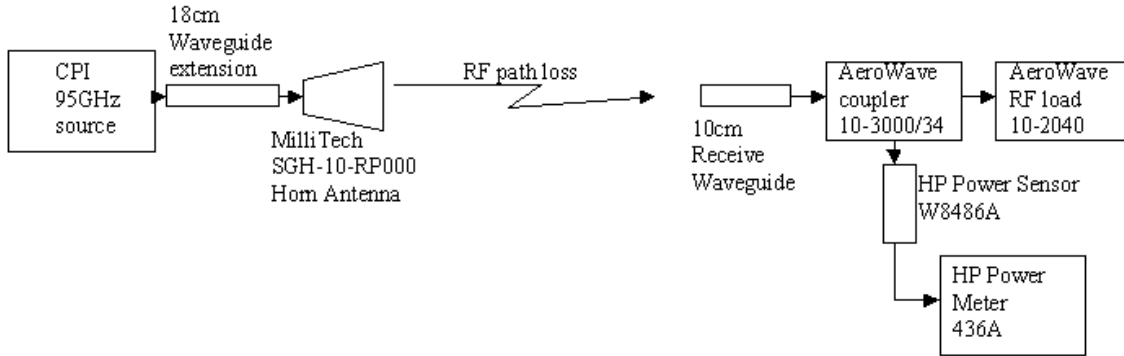


Figure 36 Power Measurement Layout

A small screen box shielded the PLL from unwanted electro-magnetic noise. A small opening in front of the screen box allowed the 95 GHz to illuminate the PLL without attenuation. Although EMI also enters the screen box through this opening, the box reduces the EMI strength sufficiently to prevent interference to the PLL.

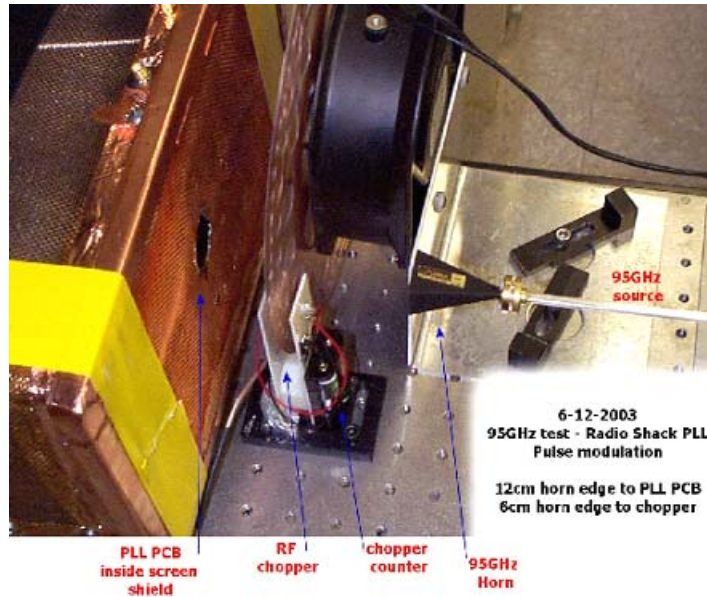


Figure 37 Setup of 95GHz Test at 12cm

Instead of monitoring the feedback error voltage to measure any VCO frequency effects, because instrumentation introduced EMI into the shield box, we measured the VCO output. We mixed the acquired VCO signal to a lower frequency and analyzed the results using Joint Time-Frequency Analysis Software (JTFA). The JTFA software is a LabVIEW routine developed to analyze how the frequency content of a waveform changes in time. A double-balanced mixer WJ-M1J mixed the 462.6625 MHz of the PLL's with 461 MHz and after low pass filtering we captured the output with a Tektronix's 5111 digital sampling oscilloscope. We also monitored the spectrum of the VCO with an Agilent Spectrum Analyzer.

Concerned that interference from sources other than the 95 GHz could affect the PLL, we carefully tested the setup for outside interference by collecting data with and without the 95 GHz source. Shown in Table 2 is the test matrix we used for this test series.

Table 2 (95 GHz Test Matrix)

Distance	RF	Chopper	Chopping Rates
12cm	Blocked	On	25 Hz, 50 Hz, 100 Hz, 250 Hz, 500 Hz, 750 Hz
22cm	Unblocked	Off	25 Hz, 50 Hz, 100 Hz, 250 Hz, 500 Hz, 750 Hz

The PLL produced a stable output except when the RF was pulsed. Figure 39 shows the JTFA plot. The variable on the abscissa is frequency. The variable on the ordinate is time.

Color in the JTFA plot represents the energy intensity. White indicates the highest energy intensity while black the least.

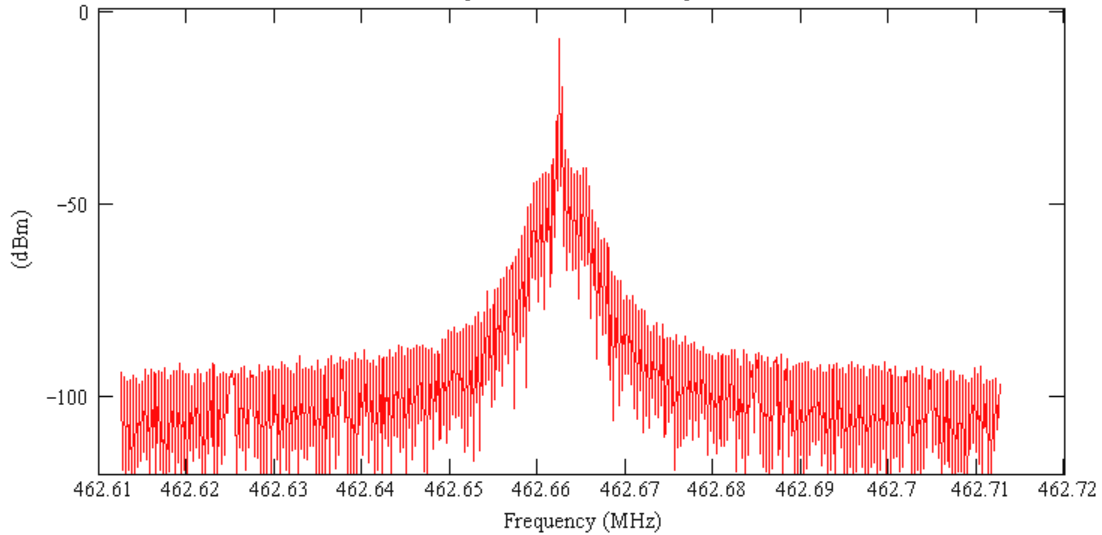


Figure 38 Spectral of PLL without 94 GHz Source

The RF pulses caused the spectral width of the VCO to widen to a spectral width of 5 to 15 kHz around the original spectrum. The spectral width is directly related to the incident power density deposited onto the VCO. The source power is fixed. Therefore, we controlled the power density on the PLL by controlling the distance between the horn and PLL. Higher power density on the VCO caused the spectral bandwidth to nearly triple from 3 kHz to 9 kHz. We used an Agilent spectrum analyzer (E4440A) to monitor the spectrum. The chopping rate did not alter the spectral content. The spectral response for the chopping rate of 200 Hz is similar to the spectral response for the 25, 50, 100, 500, 750 Hz chopping rates.

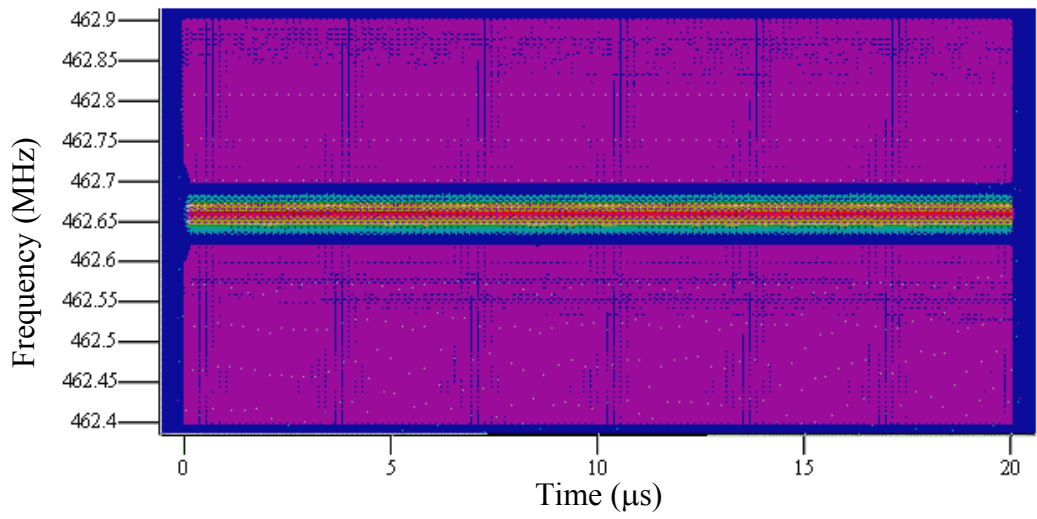


Figure 39 JTFA Results Without 94 GHz Source

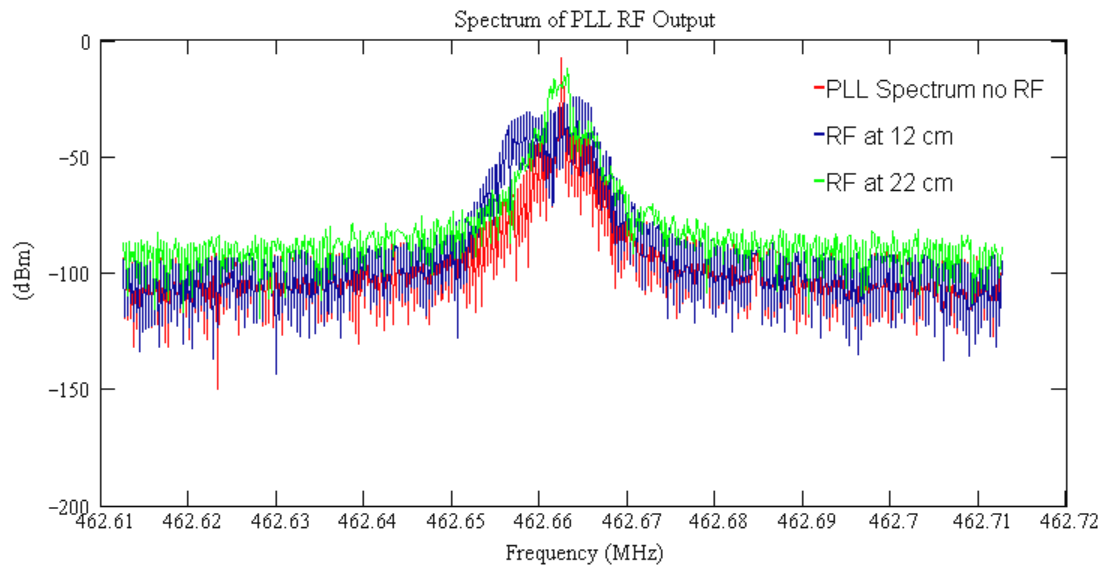


Figure 40 VCO Spectral Response with 94 GHz

Illustrated in Figure 42 through 45, the disruption period of the PLL is the same as chopping rate. The illustrations below show time windows between 20 ms and 100 ms.

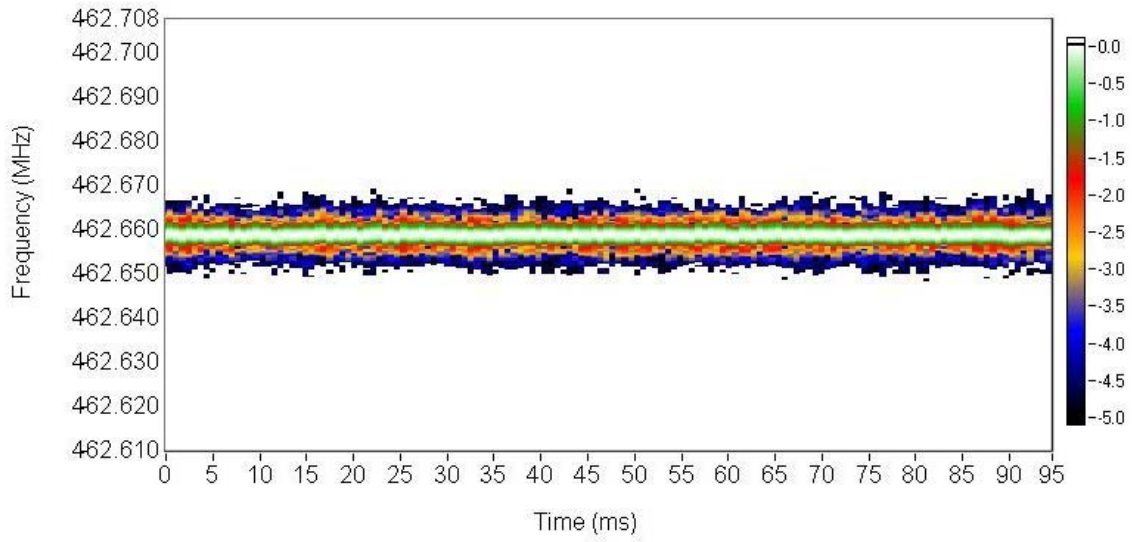


Figure 41 PLL Frequency Response Without RF

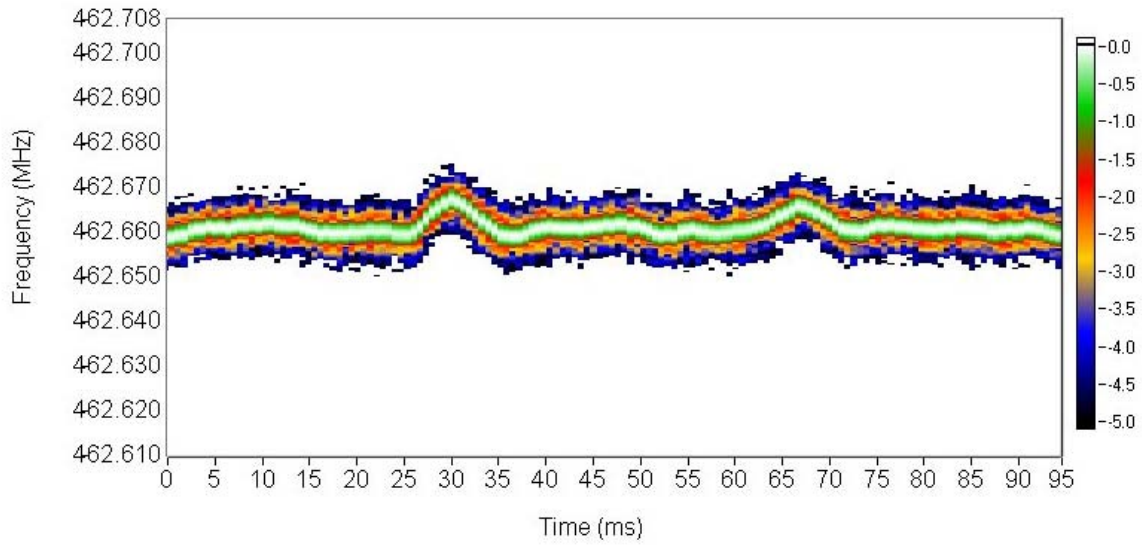


Figure 42 95 GHz PRF = 27 Hz 50% Duty Cycle

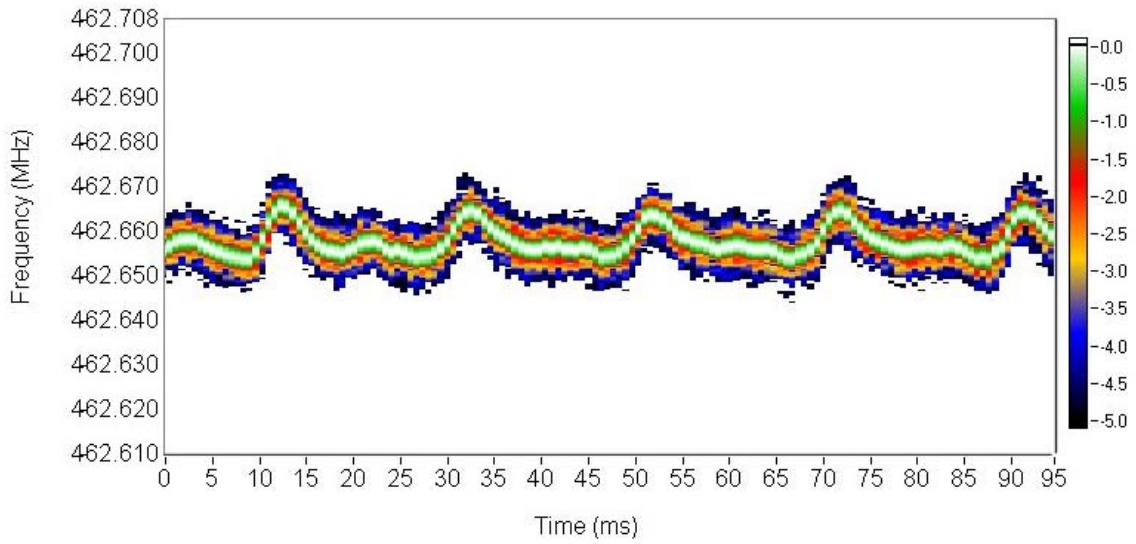


Figure 43 95 GHz PRF = 50 Hz 50% Duty Cycle

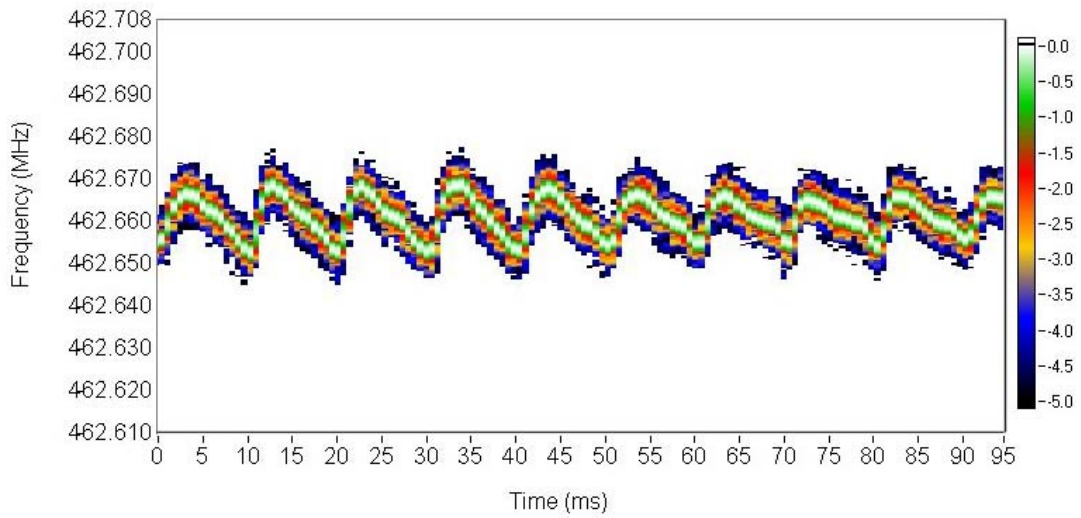


Figure 44 95 GHz PRF = 100 Hz 50% Duty Cycle

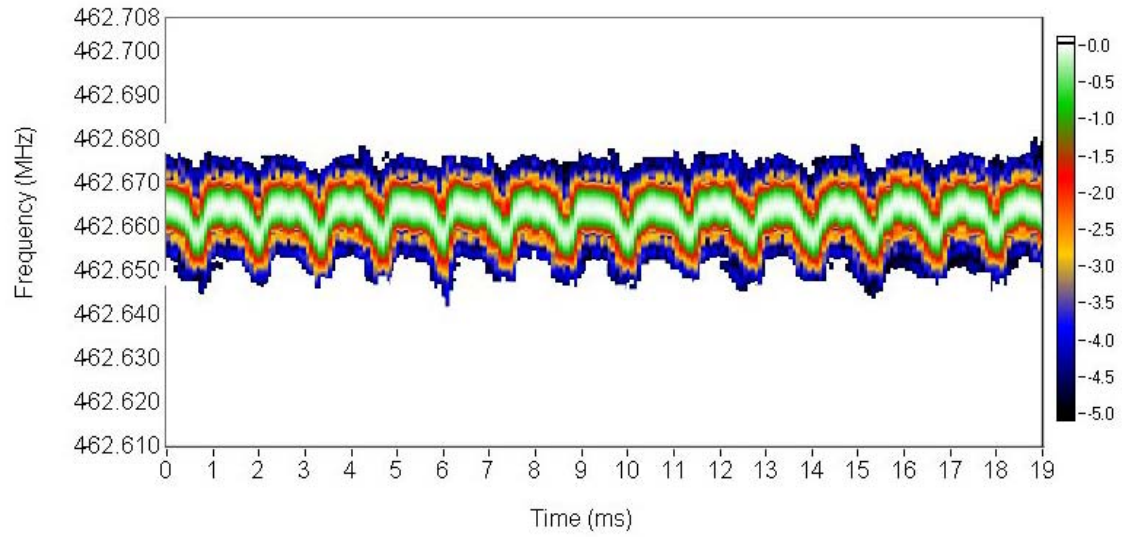


Figure 45 95 GHz PRF = 100 Hz 50% Duty Cycle

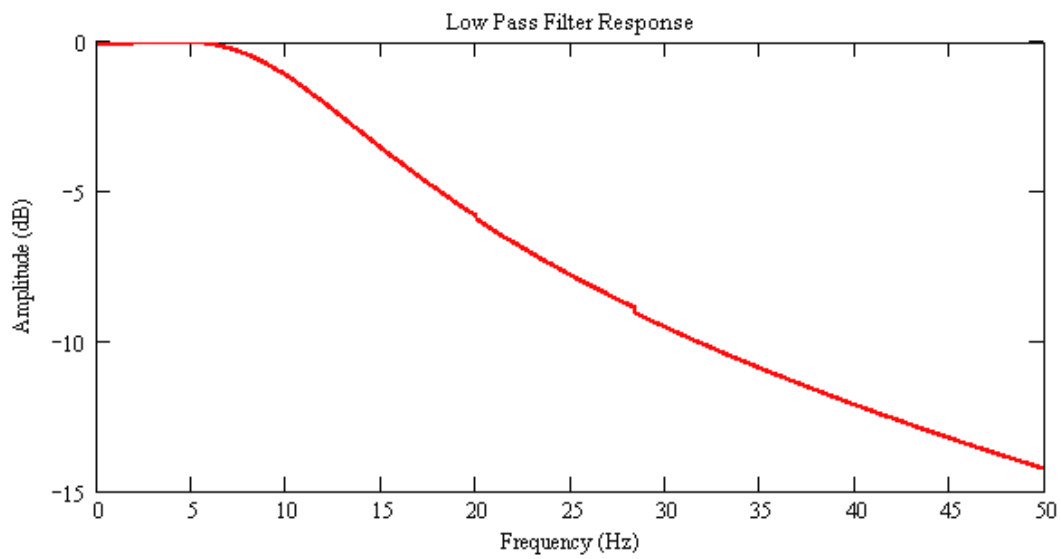


Figure 46 PLL Low Pass Filter Response

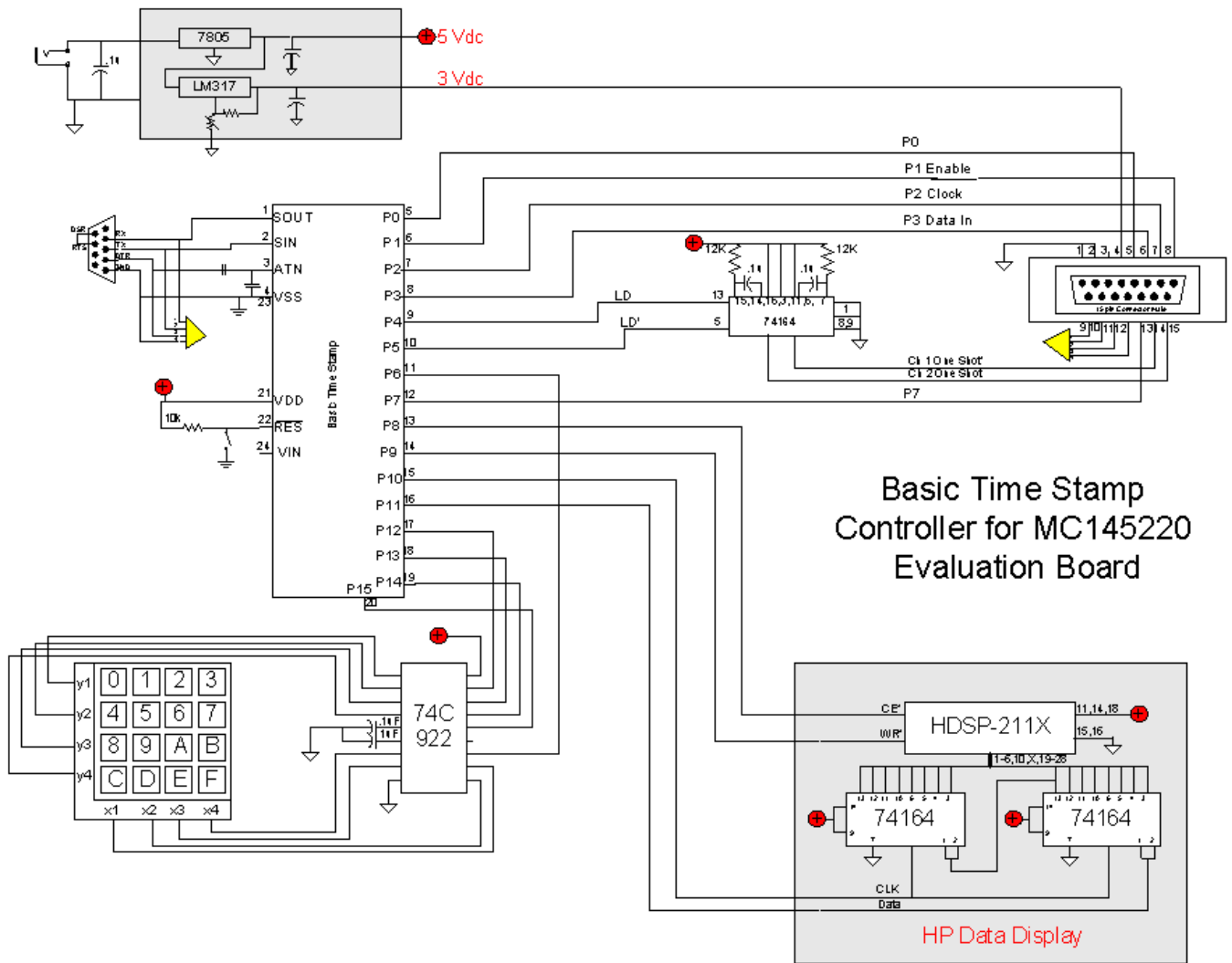


Figure 47 Motorola and PLL Controller Circuit



Figure 48 Motorola and PLL Controller

References

- ¹ “An Introduction to Chaotic Dynamical Systems”, Robert L. Devaney, pg 50
- ² “Detecting Strange Attractors in Turbulence” Lecture notes in Math Vol. 898, Springer, New York Takens, F. (1981)
- ³ M. Casdagli, T. Sauer, and J. A. Yorke. Embedology. *J. Stat. Phys.*, 65:579-616, 1991.
- ⁴ J.-P. Eckmann and D. Ruelle, Ergodic theory of chaos and strange attractors, *Rev. Mod. Phys.* 57, 617 (1985).
- ⁵ R. Stoop and J. Parisi, Calculation of Lyapunov exponents avoiding spurious elements, *Physica D* 50, 89
- ⁶ H. Kantz, A robust method to estimate the maximal Lyapunov exponent of a time series, *Phys. Lett. A* 185, 77 (1994)
- ⁷ M. T. Rosenstein, J. J. Collins, C. J. De Luca, A practical method for calculating largest Lyapunov exponents from small data sets, *Physica D* 65, 117 (1993).
- ⁸ H. Kantz and T. Schreiber, “Nonlinear Time Series Analysis”, Cambridge University Press
- ⁹ J Millman and C Halkias, “Integrated Electronics: Analog and Digital Circuits and Systems”, McGraw-Hill Book Company
- ¹⁰ Endo, Tetsur & Chua, “Chaos from Phase-Lock Loops”, *IEEE Transactions on Circuits and Systems* Vol. 35, page 987 1003. 8 August 1988
- ¹³ Ziemer, R.E. & Tranter, W.H., *Principles of Communications* John Wiley & Sons, Inc. 1995
- ¹⁴ Spectrum Software, *Micro-Cap 7.0 Reference Manual*, 7th edition 1st printing Spectrum Software, 2001
- ¹⁵ Gray, Paul R. & Meyer, Robert G., *Analysis and Design of Analog Integrated Circuits* 3rd edition John Wiley & Sons, Inc. 1993
- ¹⁶ Linsay, Paul S., *Nonlinear Dynamics in Driven and Autonomous Electronic Circuits: From Period Doubling to Systems of Multiple Oscillators* Plasma Fusion Center - Massachusetts Institute of Technology Obtained from: *Nonlinear Dynamics in Circuits* World Scientific Publishing Co., 1995
- ¹⁷ Dorf, Richard C. & Bishop, Robert H., *Modern Control Systems* 7th edition Addison-Wesley

DISTRIBUTION

Internal Distribution:

1	MS	1165	William Guyton, 15300
1		1153	Malcolm Buttram, 15330-1
1		1153	Guillermo Loubriel, 15333
1		1153	Larry Bacon, 15333
1		1153	Alan Mar, 15333
1		1153	Fred Zutavern, 15333
1		1153	Dale Coleman, 15331
1		1153	Steven Dron, 15336
10		1153	Robert A. Salazar 15333
1		1153	Luis L. Molina 15333
1	MS	9018	Central Technical Files, 8945-1
2		0899	Technical Library, 9616